

Open Research Online

The Open University's repository of research publications and other research outputs

The Lyman break analogue Haro 11: spatially resolved chemodynamics with VLT FLAMES

Journal Item

How to cite:

James, B. L.; Tsamis, Y.G.; Walsh, J. R.; Barlow, M. J. and Westmoquette, M. S. (2013). The Lyman break analogue Haro 11: spatially resolved chemodynamics with VLT FLAMES. *Monthly Notices of the Royal Astronomical Society*, 430(3) pp. 2097–2112.

For guidance on citations see [FAQs](#).

© [not recorded]

Version: Version of Record

Link(s) to article on publisher's website:
<http://dx.doi.org/doi:10.1093/mnras/stt034>

Copyright and Moral Rights for the articles on this site are retained by the individual authors and/or other copyright owners. For more information on Open Research Online's data [policy](#) on reuse of materials please consult the policies page.

oro.open.ac.uk

The Lyman break analogue Haro 11: spatially resolved chemodynamics with VLT FLAMES^{*}

B. L. James,^{1,2†} Y. G. Tsamis,^{3†} J. R. Walsh,³ M. J. Barlow⁴ and M. S. Westmoquette³

¹Space Telescope Science Institute, Baltimore, MD 21218, USA

²Institute of Astronomy, University of Cambridge, Madingley Road, Cambridge, CB3 0HA, UK

³European Southern Observatory, Karl-Schwarzschild Strasse 2, D-85748 Garching bei München, Germany

⁴Department of Physics and Astronomy, University College London, Gower Street, London, WC1E 6BT, UK

Accepted 2013 January 4. Received 2012 December 20; in original form 2012 October 18

ABSTRACT

Using VLT/Fibre Large Array Multi Element Spectrograph (FLAMES) optical integral field unit observations, we present the first spatially resolved spectroscopic study of the well-known blue compact galaxy Haro 11, thought to be a local analogue to high-redshift Lyman break galaxies. Haro 11 displays complex emission line profiles, consisting of narrow (full width at half-maximum, FWHM $\lesssim 200 \text{ km s}^{-1}$) and broad (FWHM $\sim 200\text{--}300 \text{ km s}^{-1}$) components. We identify three distinct emission knots kinematically connected to one another. A chemodynamical analysis is presented, revealing that spatially resolved ionic and elemental abundances do not agree with those derived from integrated spectra across the galaxy. We conclude that this is almost certainly due to the surface brightness weighting of electron temperature in integrated spectra, leading to higher derived abundances. We find that the eastern knot has a low gas density, but a higher temperature (by $\sim 4000 \text{ K}$) and consequently an oxygen abundance ~ 0.4 dex lower than the neighbouring regions. A region of enhanced N/O is found specifically in Knot C, confirming previous studies that found anomalously high N/O ratios in this system. Maps of the Wolf–Rayet (WR) feature at 4686 \AA reveal large WR populations ($\sim 900\text{--}1500$ stars) in Knots A and B. The lack of WR stars in Knot C combined with an age of $\sim 7.4 \text{ Myr}$ suggests that a recently completed WR phase may be responsible for the observed N/O excess. Conversely, the absence of N-enriched gas and strong WR emission in Knots A and B suggests that we are observing these regions at an epoch where stellar ejecta has yet to cool and mix with the interstellar medium.

Key words: stars: Wolf–Rayet – galaxies: abundances – galaxies: dwarf – galaxies: individual: Haro 11 – galaxies: interactions – galaxies: kinematics and dynamics.

1 INTRODUCTION

Blue compact galaxies (BCGs), due to their high star-formation rates (SFR) and low metallicities, are thought to be the nearest analogues to young, starbursting galaxies at high redshift. However, unlike their distant counterparts, the proximity of BCGs provides us with an opportunity to study galaxy evolutionary processes in great detail.

Haro 11 (ESO 350-IG 038) is a well-known member of this galaxy class, having been studied in detail in X-ray, UV, optical and infrared wavelengths (e.g. Bergvall et al. 2000; Östlin et al. 2001; Kunth et al. 2003; Hayes et al. 2007; Adamo et al. 2010; Cormier

et al. 2012). It is a massive BCG that consists of three main knots (Fig. 1), each containing numerous super star clusters with ages between 1 and 40 Myr, and high present SFR of $\sim 22 M_{\odot} \text{ yr}^{-1}$ (Adamo et al. 2010). The stellar mass was estimated as $10^{10} M_{\odot}$ by Östlin et al. (2001), whereas the total gas mass was derived by Bergvall et al. (2000) to be $2 \times 10^9 M_{\odot}$. An intriguing aspect of Haro 11 is that it is a Ly α emitting galaxy and can be considered as both a local (albeit faint) analogue of the high-redshift Lyman break galaxies (LBGs) or a rather bright Lyman alpha emitter (Hayes et al. 2007; Leitert et al. 2011). Moreover, it is also in the rare class of objects that are Lyman continuum emitters and its IR luminosity of $\sim 2 \times 10^{11} L_{\odot}$ classes it as a luminous IR galaxy (Adamo et al. 2010).

This paper focuses on another interesting aspect of Haro 11 – its classification as a ‘high-N/O’ galaxy. The distribution of nitrogen as a function of metallicity in star-forming galaxies has often been a cause for debate, especially at intermediate metallicities

^{*}Based on observations made with European Southern Observatory (ESO) telescopes at the Paranal Observatory under programme 083.B-0336A.

†E-mail: bjames@ast.cam.ac.uk

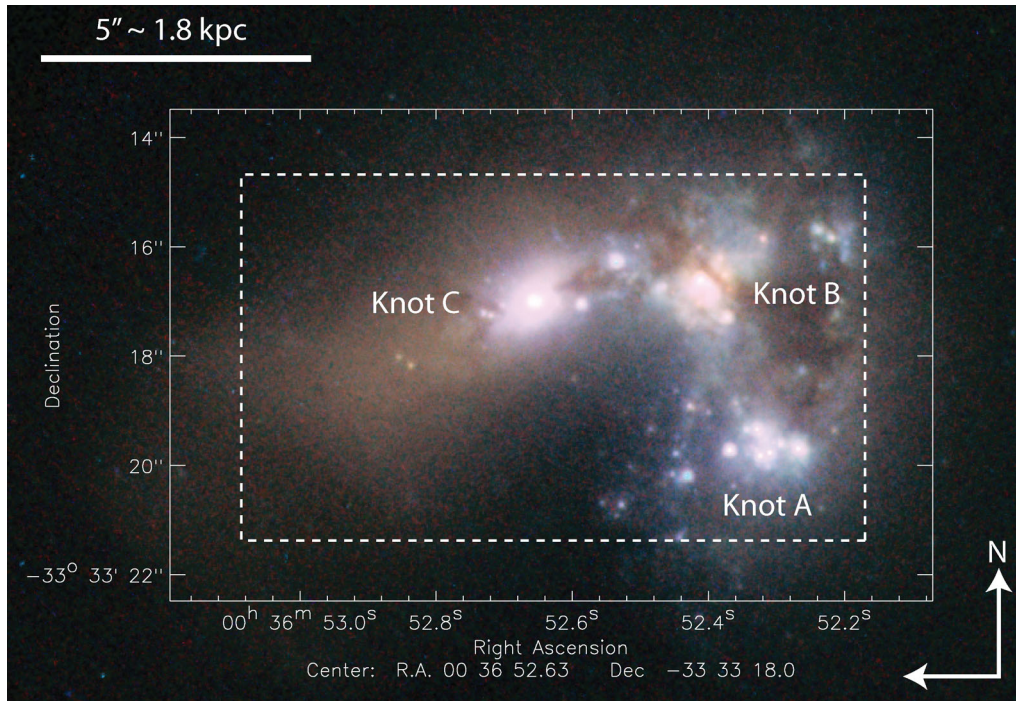


Figure 1. *HST* colour composite image of Haro 11 (consisting of ACS-HRC F220W, F330W and F814W along with ACS-WFC F435W and F550W images) overlaid with the 11.5 arcsec \times 7.3 arcsec FLAMES IFU aperture (dashed line). Knots are labelled following the nomenclature of Kunth et al. (2003).

($7.6 \leq 12 + \log(O/H) \leq 8.3$). Within this metallicity range, the N/O abundance ratio indicates that nitrogen behaves neither as a primary element (i.e. N/O is independent of O/H) nor as a secondary element (i.e. N/O is proportional to O/H); instead, a large scatter is observed (see e.g. López-Sánchez & Esteban 2010b, their fig. 11). With a nitrogen excess factor of ~ 6 for its metallicity having been reported for Haro 11 (Izotov & Thuan 1999), this galaxy belongs to a small subset of high- N/O galaxies highlighted by Pustilnik et al. (2004), several of which have been the focus of our integral field spectroscopic (IFS) observations (James et al. 2009, 2013; James, Tsamis & Barlow 2010), aimed at understanding the source of such abundance peculiarities. In the past, long-slit chemical abundance studies have suggested that a connection exists between anomalously high N/O ratios and Wolf-Rayet (WR) stars, based on their simultaneous detection. However, spatially resolved abundance studies are showing that this is not a one-to-one relationship (e.g. Monreal-Ibero, Walsh & Vílchez 2012). IFS observations of high- N/O galaxies have distinct advantages. By mapping the electron temperatures (T_e) one avoids measuring integrated and therefore likely inappropriately flux-weighted line ratios, enabling more accurate chemical abundances to be computed (e.g. Kobulnicky, Kennicutt & Pizagno 1999; James et al. 2010, 2013; Pilyugin et al. 2012). Secondly, the data allow one to isolate regions of enrichment, and thirdly, these regions can be related to environmental factors such as WR populations, large-scale outflows, mergers, etc. (Walsh & Roy 1989; López-Sánchez et al. 2007; James et al. 2009; Pérez-Montero et al. 2011; Monreal-Ibero et al. 2012).

Haro 11 is known to be a complex system. Its dynamics based on the $H\alpha$ emission have been studied by Östlin et al. (2001), who reported a multi-component velocity field and a perturbed morphology. These have been interpreted as signatures of a merger between a low-mass, evolved system and a gas-rich component. Bergvall & Östlin (2002) detected strong emission from WR stars in the spectral region around $He\ II\ \lambda 4686$ that suggests that Haro

11 may harbour a population of such stars, although to date this population has not been studied in detail.

In this paper, we present IFS observations which afford us a new spatiokinematic ‘3D’ view of Haro 11. The aims are threefold; first, to map the multiple gas components, secondly, to perform a chemodynamical study, i.e. determine the range of physical properties and chemical compositions for each emission line velocity component (e.g. Esteban & Vílchez 1992; James et al. 2009; Amorín et al. 2012; Hägele et al. 2012), and thirdly, to spatially relate any chemical anomalies to environmental factors. The adopted distance for Haro 11 along with several other of its properties are listed in Table 1.

2 OBSERVATIONS AND DATA REDUCTION

Observations of Haro 11 were obtained with the Fibre Large Array Multi Element Spectrograph (FLAMES; Pasquini et al. 2002) at

Table 1. General properties of Haro 11.

Property	Value	Reference
RA (J2000)	00 ^h 36 ^m 52.5	NED ^a
Dec. (J2000)	−33° 33′ 19″	NED ^a
z	0.020 558	This work
Distance (Mpc)	83.6	This work ^b
Velocity (km s ^{−1})	6146 \pm 17	This work
Stellar mass (M_{\odot})	$\sim 10^{10}$	Adamo et al. (2010)
Gas mass (M_{\odot})	2×10^9	Bergvall et al. (2000)
Cluster masses (M_{\odot})	10^3 – 10^6	Adamo et al. (2010)
Present SFR ($M_{\odot}\ \text{yr}^{-1}$)	22 ± 3	Adamo et al. (2010)
L_{IR} (L_{\odot})	1.9×10^{11}	Bergvall et al. (2000)

^aNASA/IPAC Extragalactic Database.

^bDerived for a Hubble constant of $H_0 = 73.5\ \text{km s}^{-1}\ \text{Mpc}^{-1}$ (DeBernardis et al. 2008).

Table 2. FLAMES Argus observing log.

Date	Grism	Wavelength range (Å)	Exp. time (s)	Avg. airmass	FWHM seeing (arcsec)	Standard star
03-07-2009	LR1	3620–4081	3 × 218	1.03	0.45	Feige56
..	LR2	3964–4567	4 × 235	1.02	0.55	LTT7987
..	LR3	4501–5078	3 × 218	1.02	0.48	Feige56
19-07-2009	LR6	6438–7184	4 × 600	1.02	0.64	Feige110
20-07-2009	LR1	3620–4081	4 × 218	1.16	0.71	HR5501
..	LR2	3964–4567	8 × 235	1.13	0.59	Feige110
..	LR3	4501–5078	6 × 218	1.06	0.67	Feige110
23-07-2009	LR1	3620–4081	9 × 218	1.08	0.59	Feige110
..	LR2	3964–4567	8 × 235	1.05	0.60	Feige110
..	LR3	4501–5078	6 × 218	1.04	0.68	Feige110
24-07-2009	LR6	6438–7184	4 × 600	1.08	0.79	LTT1020

Kueyen, Telescope Unit 2 of the 8.2 m VLT at ESO’s Paranal Observatory, in service mode on the dates specified in Table 2. Observations were made with the Argus integral field unit (IFU), with a field of view (FoV) of $11.5 \text{ arcsec} \times 7.3 \text{ arcsec}$ and a sampling of 0.52 arcsec per lens. In addition to science fibres, Argus has 15 sky-dedicated fibres that simultaneously observe the sky and that were arranged to surround the IFU FoV. The positioning of the IFU aperture for Haro 11 is shown overlaid on *Hubble Space Telescope* (*HST*) ACS/WFC F435W imaging in Fig. 1.

Four different low-resolution (LR) grisms were utilized: LR1 [$\lambda\lambda 3620\text{--}4081$, $24.7 \pm 0.2 \text{ km s}^{-1}$ full width at half-maximum (FWHM) resolution], LR2 ($\lambda\lambda 3964\text{--}4567$, $24.9 \pm 0.1 \text{ km s}^{-1}$), LR3 ($\lambda\lambda 4501\text{--}5078$, $24.7 \pm 0.2 \text{ km s}^{-1}$) and LR6 ($\lambda\lambda 6438\text{--}7184$, $22.2 \pm 0.3 \text{ km s}^{-1}$). This enabled us to cover all the important emission lines needed for an optical abundance analysis, as detailed in Section 3. The seeing ($0.45\text{--}0.79 \text{ arcsec}$), airmass and exposure time for each data set are detailed in Table 2. In addition to the science frames, continuum and ThAr arc lamp exposures as well as spectrophotometric standard star observations were obtained (also detailed in Table 2).

The data were reduced using the girBLDRS pipeline (Blecha & Simond 2004)¹ in a process which included bias removal, localization of fibres on the flat-field exposures, extraction of individual fibres, wavelength calibration and rebinning of the ThAr lamp exposures, and the full processing of science frames which resulted in flat-fielded, wavelength-rebinned spectra. The pipeline recipes ‘biasMast’, ‘locMast’, ‘wcalMast’ and ‘extract’ were used (cf. Tsamis et al. 2008). The frames were then averaged using the ‘imcombine’ task of IRAF² which also performed the cosmic ray rejection. The flux calibration was performed within IRAF using the tasks *calibrate* and *standard*. Spectra of the spectrophotometric stars quoted in Table 2 were individually extracted with girBLDRS and the spaxels containing the stellar emission were summed up to form a 1D spectrum. The sensitivity function was determined using SENSFUNC and this was subsequently applied to the combined Haro 11 science exposures. The sky subtraction was performed by averaging the spectra recorded by the sky fibres and subtracting this spectrum from that of each spaxel in the IFU. Custom-made scripts were then used to convert the row-by-row

stacked, processed CCD spectra to data cubes. This resulted in one science cube per grating, i.e. four science cubes for the source galaxy.

Observations of an object’s spectrum through the Earth’s atmosphere are subject to refraction as a function of wavelength, known as differential atmospheric refraction (DAR). The direction of DAR is along the parallactic angle at which the observation is made. Following the method described in James et al. (2009), each reduced data cube was corrected for this effect using the algorithm created by Walsh & Roy (1990).

3 MAPPING OF LINE FLUXES AND KINEMATICS

The distribution of H α Balmer line emission across Haro 11, which is indicative of current massive star-formation activity, was used to delineate three emission line regions surrounding the main knots of emission apparent in the *HST* ACS image (Fig. 1). Our analysis of Haro 11 is based on properties averaged over each of these three areas whose boundaries are displayed on the H α map in Fig. 2 and are labelled as Knots A, B and C following the nomenclature of Kunth et al. (2003).

Knots B and C in Fig. 1 correspond to unresolved super star clusters, with Knot B containing the youngest cluster population of mass $>8 \times 10^6 M_{\odot}$ (Adamo et al. 2010). Knot C is the brightest UV source in Haro 11 probably due to ongoing massive star-formation activity (Hayes et al. 2007). Knot A on the other hand is resolved to a sparse population of clusters. Both Knots B and C are ringed by dust lanes and Knot B appears almost fully surrounded by a dusty spiral arm inclined to the plane of the sky. Not only the surface brightness, but also the composite structure of the lines varies considerably across Knots A, B and C (Fig. 2).

The high spectral resolution and signal-to-noise (S/N) ratio of the data allow the identification of multiple velocity components in the majority of emission lines seen in the 300 spectra of Haro 11 across the IFU aperture. Following the automated line-fitting procedures outlined in James et al. (2013, and references therein) and likelihood ratio methods described by Westmoquette, Smith & Gallagher (2011, their appendix A), we were able to find the optimum number of Gaussians required to fit each observed profile. S/N ratio maps (used for making S/N cuts) were first made for each emission line, taking the ratio of the integrated intensity of the line

¹The girBLDRS pipeline is provided by the Geneva Observatory <http://girbldrs.sourceforge.net>

²IRAF is distributed by the National Optical Astronomy Observatory, which is operated by the Association of Universities for Research in Astronomy.

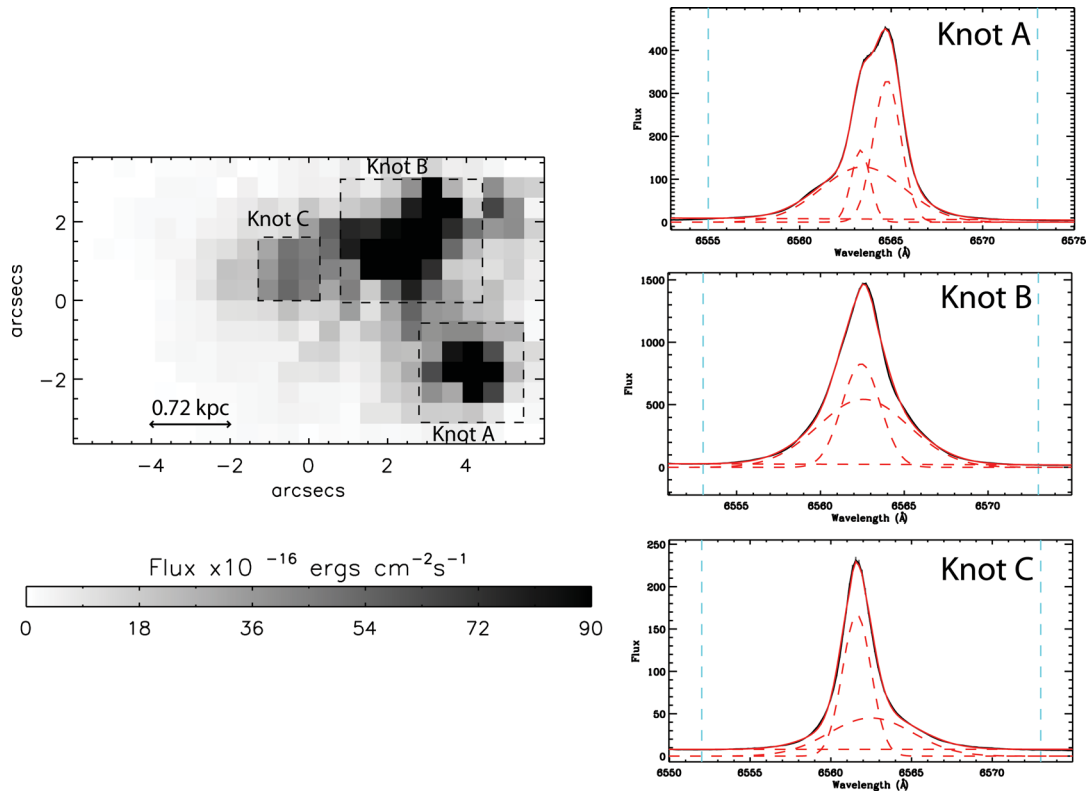


Figure 2. $H\beta$ emission per 0.52×0.52 arcsec² spaxel. Left: three regions were chosen across Haro 11 whose integrated spectra were extracted for analysis [labelled as Knots A, B and C, after the nomenclature of Kunth et al. (2003)]. Right: the $H\alpha$ line profile integrated over each region is shown along with a three-component Gaussian fit. North is up and east is to the left.

to that of the error array produced by the FLAMES pipeline,³ on a spaxel-by-spaxel basis. Single or multiple Gaussian profiles were then fitted to the emission lines, restricting the minimum FWHM to be the instrumental width (see Section 2). Suitable wavelength limits were defined for each line and continuum level fit.

Most of the high-S/N emission line profiles (i.e. all Balmer lines, [O II] $\lambda\lambda$ 3727, 3729, [O III] λ 4959,⁴ [N II] λ 6584, [S II] $\lambda\lambda$ 6716, 6731) were optimally fitted with a narrow Gaussian (FWHM < 200 km s⁻¹, component C1 hereafter), an underlying broad Gaussian component (FWHM 200–300 km s⁻¹, C2) and a third narrow Gaussian (C3 hereafter) which can appear either red- or blueshifted with respect to C1. With respect to the properties of each Gaussian component (i.e. FWHM and/or velocity), we consider them to arise from gas of different physical conditions. Towards the outer galactic regions, the lines are optimally fitted with only the C1 and C2 components. A few lines (e.g. He I λ 4026) are optimally fitted with a single, narrow component (C1). Fig. 3 shows the complex profile of the $H\alpha$ line, along with maps of its constituent velocity components.

Tables A1–A3 list measured FWHMs and observed and de-reddened fluxes for the fitted Gaussian components of the detected emission lines in the three regions defined in Fig. 2. The fluxes are for summed spectra over each star-formation knot and are

quoted relative to the flux of the corresponding $H\beta$ component. In addition, Table 3 lists the observed and de-reddened integrated line fluxes (i.e. C1+C2+C3) from summed spectra over the entire galaxy. All fluxes were corrected for reddening using the galactic reddening law of Howarth (1983) using $c(H\beta)$ values derived from the $H\alpha/H\beta$ and $H\gamma/H\beta$ line ratios of their corresponding components, weighted in a 3:1 ratio, respectively, in conjunction with theoretical Case B ratios from Storey & Hummer (1995). A Milky Way reddening of $E(B - V) = 0.011$ mag, in the direction to Haro 11, is indicated by the extinction maps of Schlegel, Finkbeiner & Davis (1998), corresponding to $c(H\beta) = 0.016$. Total $c(H\beta)$ values applicable to the galaxy and its individual emission line components in each main SF knot are listed in their respective tables.

An extinction map was also derived using the $H\alpha/H\beta$ and $H\gamma/H\beta$ emission line ratio maps and is shown in Fig. 4. This was computed using the integrated line fluxes (i.e. C1+C2+C3). The distribution in $E(B - V)$ is in agreement with that found in the Ly α study by Hayes et al. (2007), where the extinction appears to peak at the locations of Knots B and C whereas Knot A shows little or no extinction. As pointed out by Hayes et al. (2007), it is interesting that the source of Ly α emission within Haro 11 is located in Knot C, whereas one would expect a low level of extinction to be needed to allow the escape of Ly α photons. This indicates that dust is not the major regulatory factor governing the Ly α morphology in Haro 11, which was found by Hayes et al. (2007) to be driven more by the H I and kinematical structure. This is similar to what is found in many other Ly α emitting galaxies (e.g. Kunth et al. 1998; Mas-Hesse et al. 2003; Hayes et al. 2010, and references therein).

³ The uncertainties output by the pipeline include uncertainties from the flat-fielding and the geometric correction of the spectra and not just photon noise.

⁴ [O III] λ 5007 is not within the wavelength range of these data on account of its redshift.

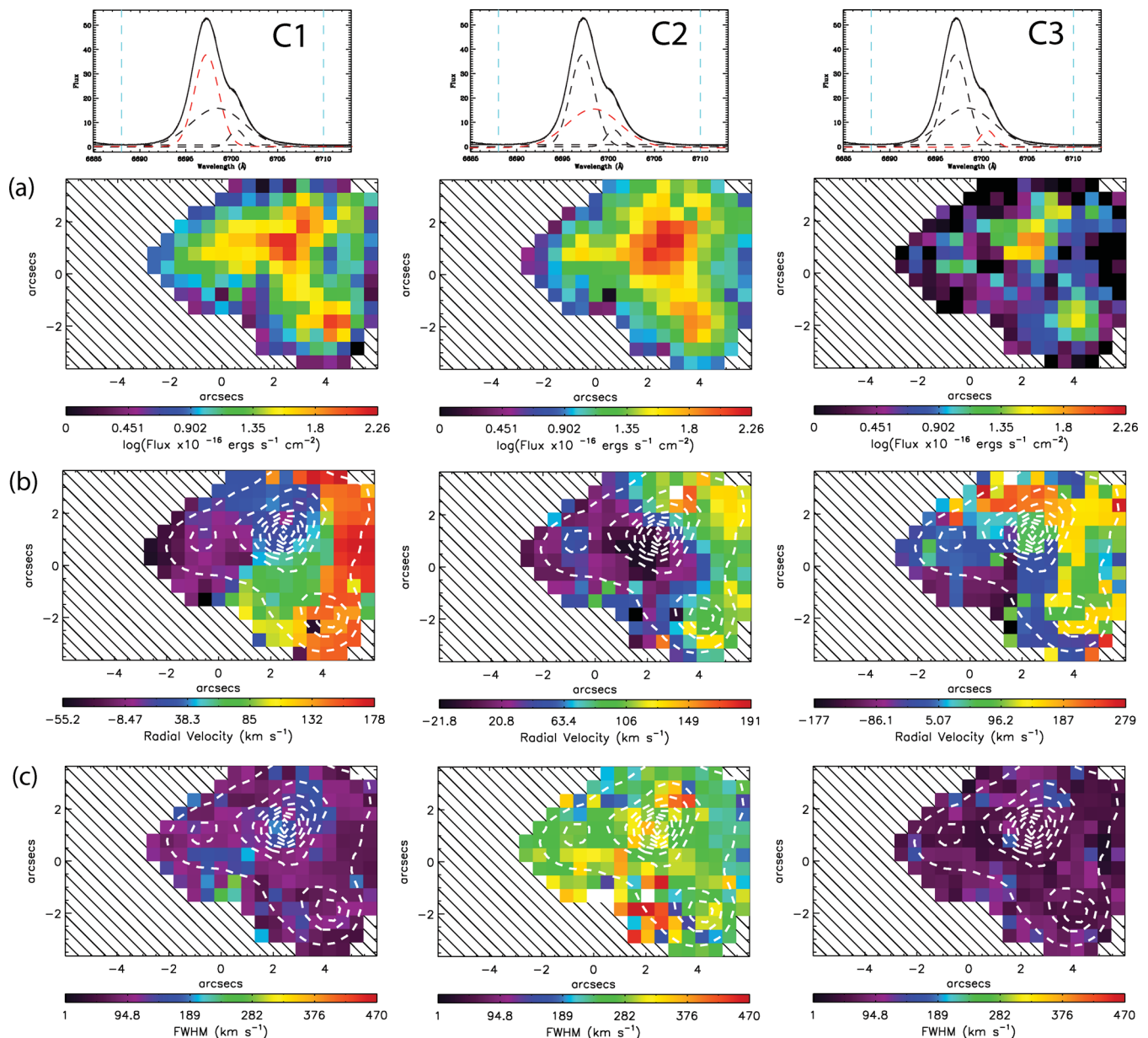


Figure 3. Maps of Haro 11 in the $H\alpha$ velocity components C1–C3. The first row shows an example three-component $H\alpha$ line profile. The highlighted component indicates to which component the maps in each column correspond; (a) logarithmic flux (in units of $10^{-16} \text{ erg s}^{-1} \text{ cm}^{-2} \text{ arcsec}^{-2}$); (b) radial velocity (relative to the heliocentric systemic velocity of 6146 km s^{-1}); (c) FWHM corrected for the instrumental point spread function. See the text for details. North is up and east is to the left.

3.1 $H\alpha$ maps

In the light of $H\alpha$ (Fig. 3a) Haro 11 consists of three main regions: a central body located at Knot B ($\alpha = 00^{\text{h}} 36^{\text{m}} 52^{\text{s}}.41 \pm 0.1$, $\delta = -33^{\circ} 33' 16''.82 \pm 0.1$, J2000), and two separated peaks, Knot C (~ 3.1 arcsec, ~ 1.2 kpc to the east) and Knot A (~ 3.2 arcsec, ~ 1.3 kpc to the south). Knots A and B are clearly evident in all three line components, with Knot B appearing most pronounced in C2. Knot C appears as a lower surface brightness feature in C1 and C2, projected against a fainter background connecting it to Knot B. The interknot background appears fainter in C3. In integrated light (C1+C2+C3), the $H\alpha$ flux of $\sim 1.06 \times 10^{-12} \text{ erg cm}^{-2} \text{ s}^{-1}$ is in reasonable agreement with Östlin et al. (1999) and Vader et al. (1993).

The $H\alpha$ radial velocity maps of Haro 11 are shown in Fig. 3b (relative to the systemic velocity). The C1 velocity component shows a velocity gradient orientated in the NE–SW direction, ranging from ~ -50 to $+100 \text{ km s}^{-1}$, and an increase up to $\sim 200 \text{ km s}^{-1}$ along the western edge. A tentative rotation axis can be defined based on component C1 which is at an angle of 90° to the dusty spiral lane surrounding Knot B in Fig. 1. In contrast to this, the velocity gradient of C2 ranges from ~ -20 to $+100 \text{ km s}^{-1}$ and extends in the NW–SE direction across Knot B, i.e. orthogonal to that of C1. This peculiar velocity structure is also highlighted by Östlin et al. (2001), who suggest that this central region contains ‘a counter-rotating disc or high-velocity blobs’, which we are tracing with component C2 and is centred on Knot B. This counter-rotating disc may also be evident as dusty filaments to the east of Knot B

Table 3. Haro 11 fluxes and de-reddened line intensities (relative $H\beta = 100$) for the integrated spectrum of Haro 11. Line fluxes were extinction-corrected using the $c(H\beta)$ value shown at the bottom of the table, calculated from the relative $H\alpha$, $H\beta$ and $H\gamma$ fluxes. The line intensities listed here were used for summed-spectra T_e and N_e diagnostics and ionic abundance calculations listed in Table 4.

Integrated spectrum	$F(\lambda)$	$I(\lambda)$
[O II] $\lambda 3727$	126.48 ± 2.66	136.59 ± 7.19
[O II] $\lambda 3729$	151.45 ± 3.16	163.56 ± 8.59
[Ne III] $\lambda 3868$	34.45 ± 1.16	36.93 ± 2.14
H8+He I $\lambda 3888$	20.81 ± 1.40	22.28 ± 1.83
He I $\lambda 4025$	1.59 ± 0.11	1.70 ± 0.14
[S II] $\lambda 4068$	2.05 ± 0.11	2.19 ± 0.15
H δ	23.21 ± 0.48	24.51 ± 1.22
H γ	43.63 ± 0.92	45.32 ± 2.18
[O III] $\lambda 4363$	2.31 ± 0.18	2.40 ± 0.21
He I $\lambda 4471$	3.55 ± 0.11	3.65 ± 0.19
[Fe II] $\lambda 4658$	1.76 ± 0.15	1.79 ± 0.17
H β	100.00 ± 2.87	100.00 ± 4.80
[O III] $\lambda 4959$	115.17 ± 3.42	114.34 ± 5.46
[O I] $\lambda 6364$	2.12 ± 0.06	1.95 ± 0.07
[N II] $\lambda 6548$	11.92 ± 0.29	10.83 ± 0.38
H α	308.67 ± 6.51	281.06 ± 9.50
[N II] $\lambda 6584$	45.42 ± 0.99	41.22 ± 1.40
He I $\lambda 6678$	2.86 ± 0.07	2.58 ± 0.09
[S II] $\lambda 6716$	25.28 ± 0.60	22.81 ± 0.79
$c(H\beta)$	0.13 ± 0.02	
$F(H\beta) \times 10^{14} \text{ erg s}^{-1} \text{ cm}^{-2}$	37.8078 ± 0.77	

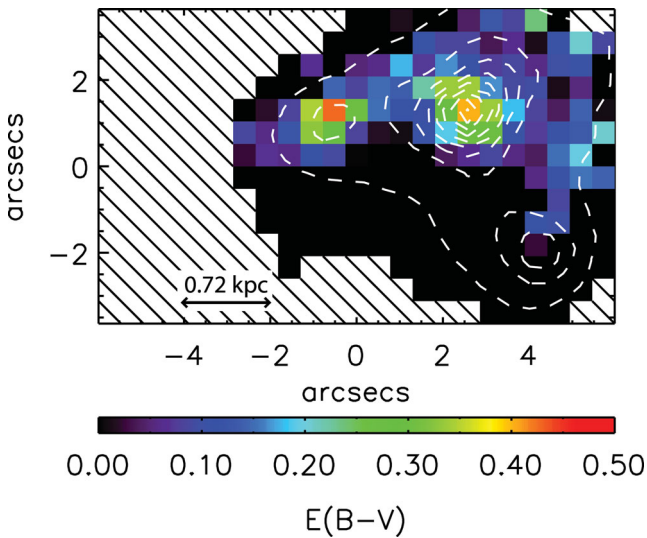


Figure 4. Map of $E(B - V)$ for the integrated flux of the emission lines. $H\alpha$ contours are overlaid in white. North is up and east is to the left.

cutting across the spiral that is ringing it (Fig 1). Overall, and in accordance with the conclusions of Östlin et al. (2001), the combined velocity distributions of C1 and C2 suggest that the centre of Haro 11 is not dynamically relaxed, while the outer velocity field shows a rather slow rotation. Component C3 shows a more patchy velocity distribution but there is evidence for a wide-angled bipolar outflow oriented approximately along the north–south direction centred on Knot B. The overall velocity distribution of C3 could also be interpreted as the lower S/N ratio signature of geometrically thin shells

created by stellar outflows and supernova (SN) remnants projected against the background emission.

FUSE observations of Haro 11 by Grimes et al. (2007) report similar findings to the $H\alpha$ velocity maps presented here, albeit in one dimension and relative to a slightly higher systemic velocity of 6180 km s^{-1} . UV absorption lines show strong absorption features (with FWHMs of $\sim 300 \text{ km s}^{-1}$) blueshifted by 100 km s^{-1} relative to the host galaxy systemic velocity (rather equivalent to our C2 component) and an additional, weaker high-velocity outflow $+200$ – 280 km s^{-1} away from the galaxy (our C1 component). Interestingly, when comparing the equivalent widths (EW), the higher ionization UV lines are stronger in the high-velocity outflow than the low-velocity absorption features, which Grimes et al. (2007) suggest could be due to shocks between the outflow and the ambient material.

The maps of $H\alpha$ FWHM (Fig. 3c) show minimal structure in each of the three main velocity components. FWHMs are in the ranges ~ 80 – 180 km s^{-1} for C1, ~ 180 – 450 km s^{-1} for C2 and $< 90 \text{ km s}^{-1}$ for C3. Östlin et al. (2001) observe a maximum FWHM of $\sim 270 \text{ km s}^{-1}$ for the emission lines within Haro 11, which agrees well with the average FWHM of $283 \pm 5 \text{ km s}^{-1}$ seen for C2 throughout the main body of the galaxy. The largest FWHM value for C2 is observed directly east of Knot A coinciding with a super star cluster positioned at the end of a bright arc of emission extending southwards from Knot B (Fig. 1). This region spatially aligns with a region of blueshifted C3 emission and could thus be a further signature of outflow activity originating in Knot B.

3.2 Forbidden lines

Emission line maps of Haro 11 in the light of the [O III], [N II], [S II] and [Ne III] lines are shown in Fig. 5. The morphology of [O III] $\lambda 4959$ is similar to that of $H\alpha$, with the peak in C2 emission being more extended than that of C1. Despite the low S/N of the [O III] $\lambda 4363$ line, we were able to map the C1 velocity component throughout Haro 11, with peaks that correlate with those in $H\alpha$ along with the C2 component within Knot B.

We show Haro 11 in the light of [S II] $\lambda 6716$ emission in Fig. 5d, in the C1 and C2 velocity components. Unlike the C1 components of the [N II] and [O III] emission lines, [S II] $\lambda 6716$ does not show clear peaks in surface brightness, but instead remains relatively constant throughout the main body of Haro 11. In comparison, the C2 velocity component of [S II] $\lambda 6716$ peaks strongly in Knot B with a morphology akin to $H\alpha$ C2 emission (Fig. 3a – central panel). Fig. 5e shows Haro 11 in the light of [Ne III] $\lambda 3868$, which was only present in a narrow (C1) component, that has three clear peaks at the three main knots of star formation.

Fig. 6 shows Haro 11 in the light of the electron density (N_e) sensitive doublet ratio, [O II] $\lambda\lambda 3726/3729$. A small amount of structure is visible; the ratio peaking at the location of Knot B, which suggests a region of increased N_e . The broad component of the [O II] $\lambda\lambda 3726, 3729$ doublet cannot be reliably decomposed as their relatively small rest wavelength separation is blurred out by its large width. The [S II] $\lambda\lambda 6716, 6731$ doublet on the other hand is unusable as at the redshift of Haro 11 the latter line falls in a spectral region of strong telluric oxygen absorption.

4 DIAGNOSTICS: ELECTRON TEMPERATURE AND DENSITY

The de-reddened [O III] ($\lambda 4959$)/ $\lambda 4363$ and [O II] $\lambda 3726/\lambda 3729$ intensity ratios were used to determine electron temperatures and

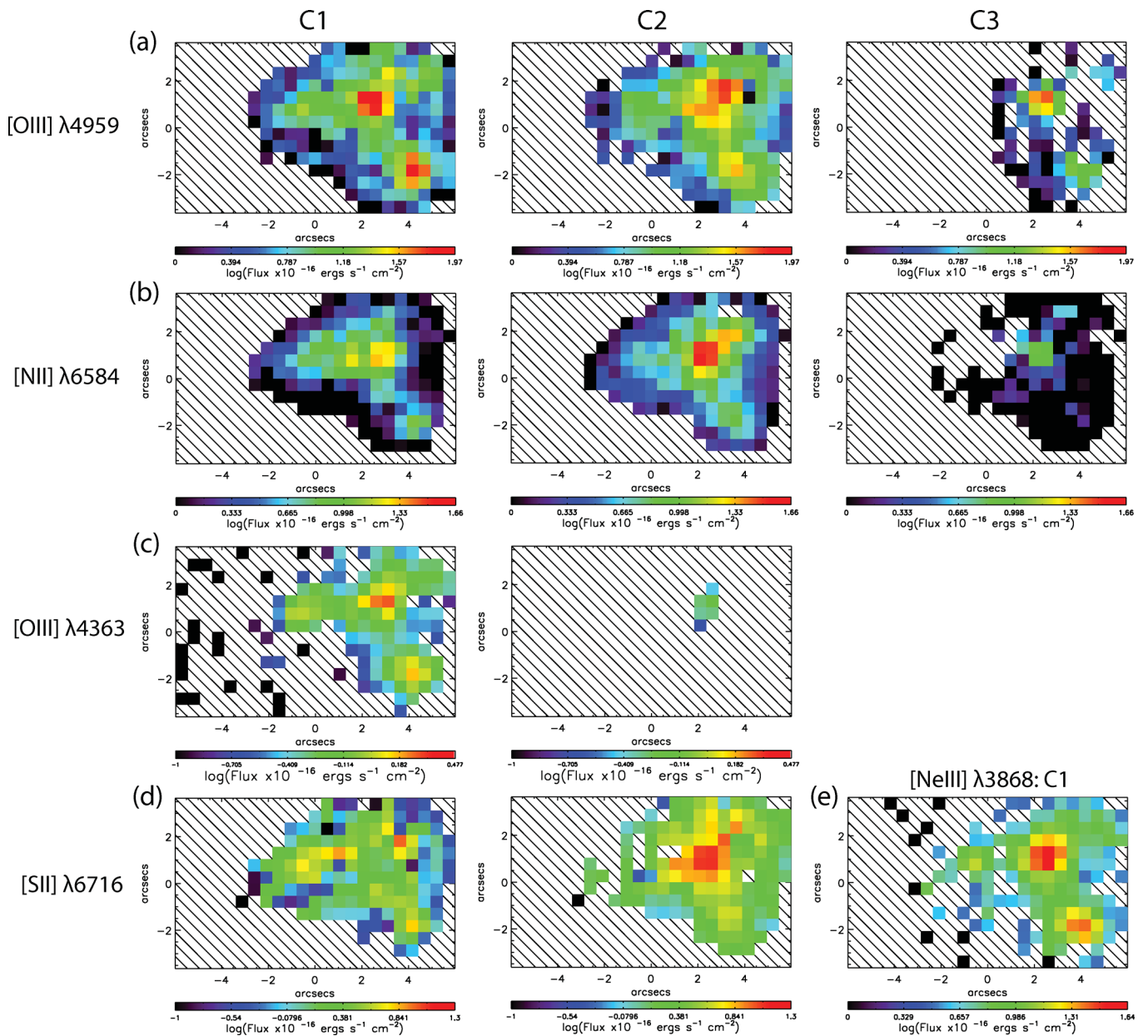


Figure 5. De-reddened intensity maps of Haro 11 in [O III] $\lambda 4959$, [N II] $\lambda 6584$, [O III] $\lambda 4363$ and [Ne III] $\lambda 3868$ for the separate velocity components C1, C2 and C3. [O III] $\lambda 4363$ is shown after being rebinned by 1.5×1.5 spaxels and remapped on to the original grid (see the text for details). Only spaxels with $S/N \geq 10$ are shown for [O III] $\lambda 4959$ and [N II] $\lambda 6584$, ≥ 5 for [Ne III] $\lambda 3868$ and ≥ 1 for [O III] $\lambda 4363$. North is up and east is to the left.

electron densities throughout Haro 11, respectively. The T_e and N_e values were computed by inputting the [O III] and [O II] intensity ratios into IRAF'S ZONES task in the NEBULA package. This task derives both the temperature and the density by making simultaneous use of temperature- and density-sensitive line ratios. Atomic transition probabilities for O^{2+} and O^+ were taken from Wiese, Fuhr & Deters (1996) whilst collision strengths were taken from Lennon & Burke (1994) and McLaughlin & Bell (1993), respectively.

T_e maps computed for line components C1 and C2 are shown in Fig. 7 and the N_e map for C1 is shown in Fig. 8. The per spaxel S/N ratio of the T_e maps is in the range 10–20. The error-weighted mean values for each of the Knots (i.e. map-based averages across apertures defined in Fig. 2) are listed in Table 4, along with uncertainties corresponding to the standard deviation across each aperture. Fig. 7a shows evidence for a small amount of T_e variation through-

out Haro 11. For component C1, Knots A and B show temperatures of ~ 12 – 13 000 K whilst Knot C shows ~ 16 000 K. The broad-line component in Knot B has a lower temperature of ~ 9000 K.

Electron density variations are also apparent and denser areas are correlated with Knots A and B which show densities of ~ 400 cm^{-3} whereas Knot C is less dense with ~ 150 cm^{-3} . The low N_e seen in Knot C may help explain the escape of $\text{Ly}\alpha$ photons within this region (Hayes et al. 2007). In Knot C, Hayes et al. (2007) found that the $\text{Ly}\alpha/\text{H}\alpha$ ratio agrees with the theoretical Case B recombination value, $\text{Ly}\alpha/\text{H}\alpha = 8.7$ (Osterbrock & Ferland 2006), indicating that the $\text{Ly}\alpha$ photons from this region are scattered just a few times before escaping. Such direct escape would be possible from a low-density, dust-poor nebula bordering on the optically thin Case A; however, as we discussed in the introduction to Section 3, the dust content is probably not the determinant factor in this case, the lower

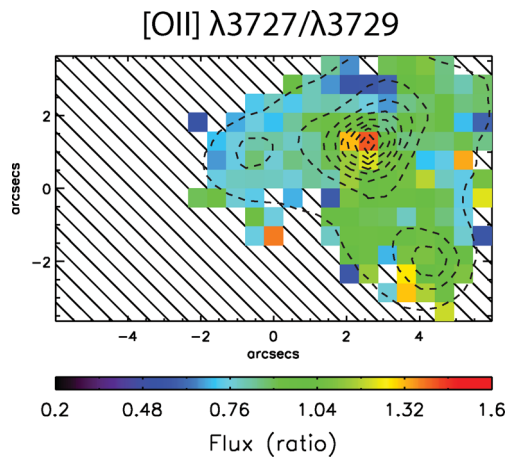


Figure 6. De-reddened emission line maps of Haro 11 in [O II] $\lambda 3726/\lambda 3729$, with integrated light H α emission line contours overlaid in dashed lines. North is up and east is to the left.

density may be the cause. As suggested by the models of Neufeld (1991), Ly α photons will suffer less attenuation than radiation that is not resonantly scattered when they exist in a multi-phase medium, i.e. dusty gas clouds embedded within a low-density intercloud medium. Our N_e values based on the C1 [O II] $\lambda 3726/\lambda 3729$ ratio are not in agreement with that of Guseva et al. (2012); this may be because their [S II] diagnostic is affected by telluric absorption of the $\lambda 6731$ component.

5 CHEMICAL ABUNDANCES

Ionic abundance maps relative to H $^+$ were created for the N $^+$, O $^+$, O $^{2+}$, Ne $^+$ and S $^+$ ions, using the $\lambda\lambda 6584, 3727+3729, 4959, 3868$ and 6717 lines, respectively. Examples of flux maps used in the derivations of these ionic abundance maps can be seen in Fig. 5. Abundances were calculated using the *zones* task in IRAF, using the respective T_e and N_e maps described above, with each FLAMES spaxel treated as a distinct ‘nebular zone’ with its own set of phys-

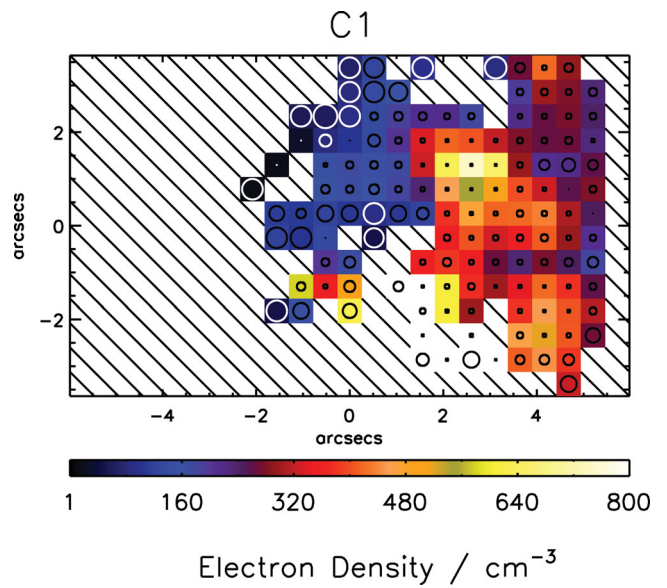


Figure 8. Electron density map of Haro 11 for the velocity components C1 and C2. Overlaid circles represent the size of the uncertainty in T_e within each spaxel. North is up and east is to the left.

ical conditions. The IRAF abundance results are corroborated by comparing with abundance maps computed via the program EQUIB (originally written by I. D. Howarth and S. Adams), which uses different atomic data tables; we found that typically the differences in the abundance ratios are within 5 per cent.

Ionic nitrogen, neon and sulphur abundances were converted into N/H, Ne/H and S/H abundances using ionization correction factors (ICFs) from Kingsburgh & Barlow (1994). The O/H abundance was obtained by adding the O $^{2+}/H^+$ and O $^+/H^+$ abundance maps (i.e. assuming that the O $^{3+}/H^+$ ratio is negligible). Since the [S III] $\lambda 6312$ line was not within the wavelength range of our data, the S $^{2+}/H^+$ abundance was estimated using the empirical relationship between the S $^{2+}$ and S $^+$ ionic fractions from the corrected equation A38 of Kingsburgh & Barlow (1994), namely S $^{2+}/S^+$

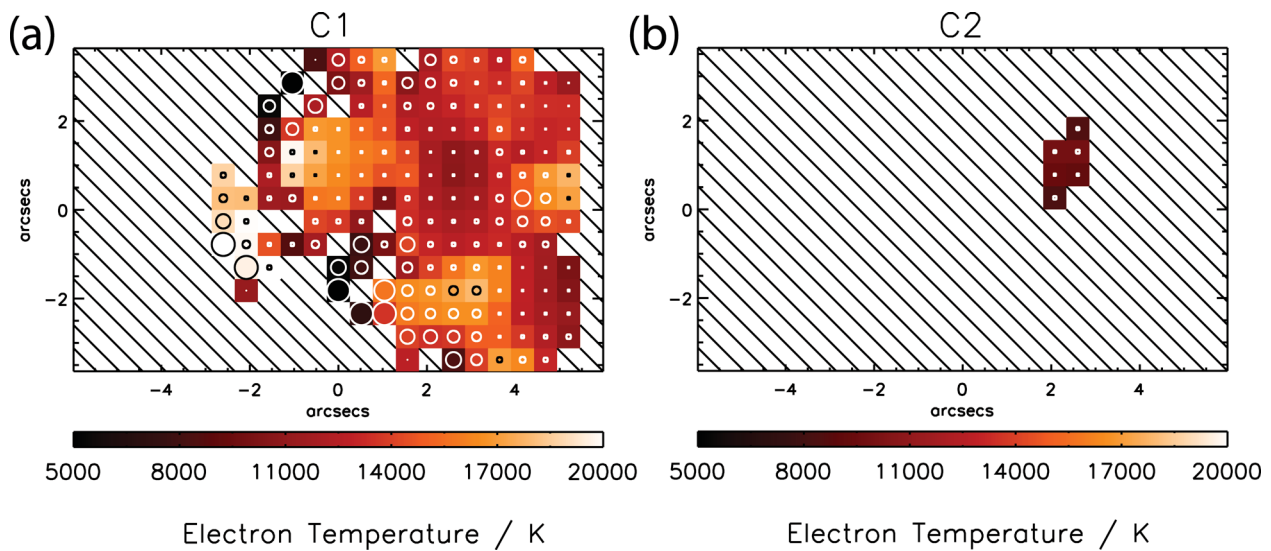


Figure 7. Electron temperature map of Haro 11 for the velocity components C1 and C2. Overlaid circles represent the size of the uncertainty in T_e within each spaxel. North is up and east is to the left.

Table 4. Ionic and elemental abundances for Haro 11, with the corresponding T_e and N_e used in their derivation. Columns 1–4 refer to abundances derived from maps, weight-averaged over regions defined in Fig. 2. All ionization correction factors (ICFs) are taken from Kingsburgh & Barlow (1994).

	C1		Knot C	C2	Summed spectra
	Knot A	Knot B		Knot B	
T_e	$12\,600 \pm 270$	$12\,100 \pm 230$	$16\,600 \pm 480$	9000 ± 400	$10\,340 \pm 440$
N_e	410 ± 20	370 ± 10	150 ± 15	–	180 ± 100
$O^+/H^+ \times 10^5$	5.64 ± 0.85	10.92 ± 1.28	3.91 ± 0.39	–	1.34 ± 0.07
$O^{++}/H^+ \times 10^5$	6.78 ± 0.84	6.92 ± 0.69	2.45 ± 0.22	15.38 ± 2.71	1.19 ± 0.06
$O/H \times 10^4$	1.24 ± 0.24	1.78 ± 0.27	0.64 ± 0.08	–	2.53 ± 0.18
$12+\log(O/H)$	8.09 ± 0.20	8.25 ± 0.15	7.80 ± 0.13	–	8.40 ± 0.07
Z/Z_\odot	0.24 ± 0.05	0.35 ± 0.05	0.12 ± 0.02	–	0.49 ± 0.04
$N^+/H^+ \times 10^6$	2.19 ± 0.22	5.74 ± 0.43	3.00 ± 0.21	20.28 ± 2.74	8.16 ± 0.28
ICF(N)	2.20	1.63	1.63	–	1.89
$N/H \times 10^6$	4.82 ± 1.28	9.38 ± 1.95	4.88 ± 0.88	–	15.45 ± 1.49
$\log(N^+/O^+)$	-1.41 ± 0.08	-1.28 ± 0.06	-1.12 ± 0.05	–	-1.21 ± 0.03
$Ne^{++}/H^+ \times 10^5$	2.62 ± 0.34	3.93 ± 0.48	1.36 ± 0.13	3.75 ± 0.22	
ICF(Ne)	1.83	2.58	2.59	–	2.12
$Ne/H \times 10^5$	4.79 ± 1.27	10.14 ± 2.23	3.54 ± 0.66	–	7.94 ± 0.83
$\log(Ne^{2+}/O^{2+})$	-0.41 ± 0.14	-0.25 ± 0.12	-0.25 ± 0.10	–	-0.50 ± 0.03
$S^+/H^+ \times 10^7$	3.37 ± 0.32	4.64 ± 0.34	6.36 ± 0.49	18.47 ± 2.48	8.79 ± 0.55
ICF(S)	1.06	1.02	1.02	–	1.04
$S/H \times 10^7$	21.71 ± 5.35	22.93 ± 4.44	31.25 ± 5.19	–	4.97 ± 0.26
$\log(S^+/O^+)$	-1.76 ± 0.14	-1.89 ± 0.11	-1.31 ± 0.09	–	-2.18 ± 0.04

$= 4.677 \times (O^{2+}/O^+)^{0.433}$. The S/H results should therefore be considered with caution, but they are not at variance with those obtained using the ICF prescriptions of Izotov et al. (2006). O/H, N/H and $\log(N/O)$ abundance maps for line component C1 are shown in Fig. 9 and are described below. Abundances for the three regions were derived from taking error-weighted averages across the regions in the abundance maps shown in Fig. 9. These map-based spatial averages are listed in Table 4 and correspond to the ‘average values’ described in the following section. We were unable to derive ICFs for the C2 line component without maps of [O II]-C2; however, averages over the ionic abundance maps are listed in Table 4.

5.1 Maps

The elemental oxygen abundance map shown in the top panel of Fig. 9 displays a single peak whose location correlates with Knot B (the brightest of the knots in terms of $H\alpha$ flux). Both Knots A and C reveal a decreased oxygen abundance at the location of their peak in $H\alpha$ flux. Slight abundance variations are seen across Haro 11, with a decreasing oxygen abundance as one moves away from Knot B, with an average metallicity of $12+\log(O/H)=8.25 \pm 0.03$, decreasing to 8.09 ± 0.03 and 7.80 ± 0.04 for Knots A and C, respectively. There is, therefore, a distinct inhomogeneity in oxygen abundance across Haro 11, with Knot B having a higher oxygen abundance by up to ~ 0.4 dex. Whilst the result for Knot B is in relatively good agreement with Guseva et al. (2012) who derived $12+\log(O/H)=8.33$, our abundance for Knot C is somewhat lower than their 8.10 due to our higher temperature (they derive $\sim 11\,500$ K for Knot C). We are, however, in agreement with the value $12+\log(O/H)=7.9$ obtained by Bergvall & Östlin (2002) in a $4\text{ arcsec} \times 4\text{ arcsec}$ aperture over the brightest region of Haro 11 in the visual region. Whilst we cannot comment on the C2 elemental abundance of oxygen, Table 4 shows that the O^{2+} C2 component

abundance in Knot B is approximately twice that of its narrow C1 component.

The middle panel of Fig. 9 shows the N/H abundance across Haro 11. The peak in abundance is located within Knot B, with an average N/H ratio of $9.38 \pm 0.02 \times 10^{-6}$, which decreases to $\sim 4.88 \times 10^{-6}$ in Knots A and C. In contrast to oxygen, there is no distinct decrease in nitrogen abundance in Knot C and as a result this knot shows a peak in N/O, which can be seen in the bottom panel of Fig. 9. Whilst Knots A and B display relatively ‘normal’ $\log(N/O)$ levels for their respective metallicities (~ -1.4 and -1.3 ; see López-Sánchez & Esteban 2010b, their fig. 11), Knot C has an average $\log(N/O)$ of -1.12 , ~ 0.5 dex higher than the expected value for $12+\log(O/H)=7.80$. In fact, the map of $\log(N/O)$ shows that this peak actually reaches ~ -1.0 to -0.8 at the boundary between Knots B and C (as can be seen by the $H\alpha$ contours). Therefore, the factor of ~ 3 excess reported by Pustilnik et al. (2004) is seen by us within Knot C only. We investigate the cause behind this anomalously high ratio in Section 6.

Again, we cannot draw firm conclusions on the N/H or N/O abundance within the broad velocity component gas. However, as a rough estimate, if we apply the average ratio of $O^+/O^{2+}=1.57$ seen in the C1 component of Knot B to the O^{2+}/H^+ value in C2, we would obtain $O^+/H^+=2.43 \times 10^{-4}$ and a $\log(N^+/O^+)$ ratio of -1.07 . This would provide some evidence for the existence of a broad-line region within Knot B that has a higher O/H abundance than the narrow-line component, but a similar N/O ratio.

Guseva et al. (2012) derive $\log(N/O)$ values of -0.92 and -0.79 for Knots B and C, respectively; whilst the value for Knot C is in agreement with the maps derived here, the value for Knot B is somewhat higher. We interpret this as being a result of their using ratios from integrated line profiles.

The Ne/H distribution in Haro 11 (not shown) follows that of nitrogen in that a peak in abundance is seen in Knot B with $Ne/H=1.0 \times 10^{-4}$, whilst Knots A and C have an abundance ratio of

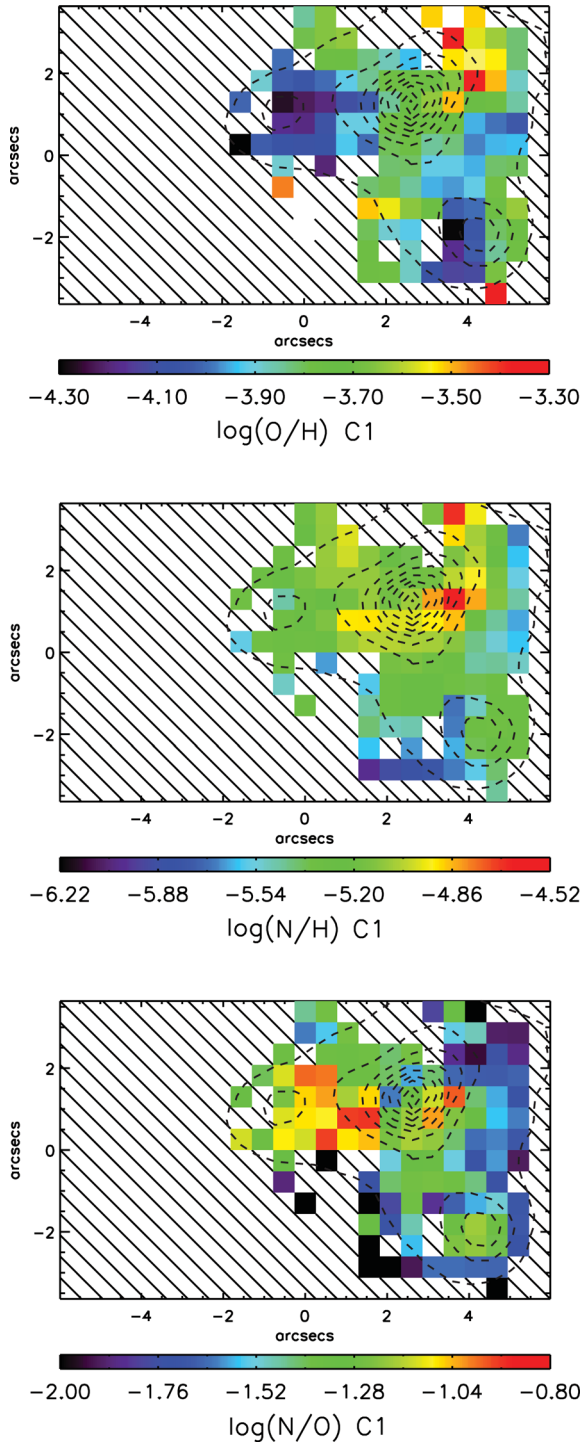


Figure 9. Elemental nitrogen, oxygen and N/O abundance maps for the velocity component C1, with integrated light $H\alpha$ emission line contours overlaid in dashed lines. North is up and east is to the left.

$\sim 0.4 \times 10^{-4}$. The average Ne/O ratios are all ~ 0.4 dex higher than the expected range of $\log(\text{Ne/O}) \sim -0.9$ to -0.4 (López-Sánchez & Esteban 2010b). Derivations of Ne/H were also made using the neon ICF of Izotov et al. (2006), with only the Ne/O ratio for Knot B being ~ 0.1 dex higher than the expected value. The S/H distribution across Haro 11 (also not shown) is relatively constant for the C1 gas component, with each region displaying averages within the range of $\sim (3-6) \times 10^{-7}$. The S/O ratio for Knot C is in agreement with the

average reported range of $\log(\text{S/O}) \sim -1.9$ to -1.5 (Izotov et al. 2006) for BCGs, whilst Knots A and B are $\sim 0.2-0.4$ dex lower than the expected values.

5.2 Comparison of spatially resolved and global spectra abundances

Also listed in Table 4 are the T_e , N_e , ionic and elemental abundances derived from the galaxy integrated spectra (using the line fluxes listed in Table 3). Following the methodology of James et al. (2013), this set of results allows us to assess if integrated galaxy spectra can reliably represent the physical properties of the ionized interstellar medium (ISM). In a comparison between spatially averaged and integrated-spectra results for UM 448, James et al. (2013) found that whilst *relative* abundance ratios of heavy elements can be reasonably well obtained from integrated spectra and/or long-slit observations, the ionic and elemental abundances relative to hydrogen are not well reproduced. James et al. (2013) suggested that this may be because the former properties do not have a very strong sensitivity to T_e biases and/or, in contrast to integral field spectroscopy, integrated properties derived from flux-averaged methods cannot resolve abundance and temperature variations and sites of enrichment are being averaged out.

The present results suggest that whilst the N/O and Ne/O values are in agreement with the spatially averaged values, the ionic and elemental abundance ratios relative to hydrogen are not. The T_e from the integrated spectrum is in excellent agreement with the $\lambda 4959$ -flux-weighted mean T_e across the three regions (10 850 K), suggesting that the integrated [O III] ratio may have been more heavily weighted by areas of stronger [O III] $\lambda 4959$ emission. Indeed, the average T_e for Knot B (which has the strongest [O III] emission) from the C1 and C2 maps would be $\sim 10 550$ K – in agreement with the integrated-spectrum T_e . These discrepancies suggest that values derived from long-slit observations may be prone to luminosity-weighted fluxes and resultant inaccurate ratios, compounded by the fact that large apertures can include a mixture of gas with different ionization conditions and metal content. Such effects can lead to significant biases in analyses based on the integrated spectra of galaxies both in the local and the high-redshift Universe. These biases may be of comparable magnitude to the effects of temperature or density variations (e.g. Peimbert & Costero 1969; Rubin 1989; Viegas & Clegg 1994) often invoked in nebular abundance analyses.

5.3 Helium abundances

The He^+/H^+ abundances for Knots A and B are listed in Table 5. The He I lines in Knot C are abnormally weak relative to $\text{H}\beta$ probably due to the effects of underlying stellar absorption, and hence a reliable He abundance cannot be derived for this area. Summed spectra over each knot and velocity component (i.e. C1+C2+C3) were used rather than map-based averages because of the low per spaxel S/N ratio of the lines. Fluxes were de-reddened using the $c(\text{H}\beta)$ value for its corresponding knot. Helium abundances were calculated using the error-weighted line fluxes listed in Table 6 and adopting the map-based average T_e and N_e for each knot (listed in Table 4). The Case B He I emissivities of Smits (1996) were adopted, correcting for the effects of collisional excitation using the formulae in Benjamin, Skillman & Smits (1999). The presence of neutral helium within the H^+ zone has been accounted for using the ICF of Peimbert, Torres-Peimbert & Ruiz (1992). No substantial amounts of He^{2+} are expected to be present.

Table 5. Regional He/H abundances for Knots A and B from integrated line fluxes (here in units relative to $H\beta = 100$) summed over the regions defined in Fig. 2.

	Knot A		Knot B	
	$F(\lambda)$	$I(\lambda)$	$F(\lambda)$	$I(\lambda)$
He I $\lambda 4471$	3.22 ± 0.12	3.23 ± 0.22	3.93 ± 0.21	4.16 ± 0.29
He I $\lambda 6678$	3.10 ± 0.21	3.09 ± 0.23	3.55 ± 0.10	2.89 ± 0.11
$c(H\beta)$	0.01 ± 0.01		0.27 ± 0.02	
$He^+/H^+ \times 10^2$ ($\lambda 4471$)	6.53 ± 0.41		8.31 ± 0.58	
$He^+/H^+ \times 10^2$ ($\lambda 6678$)	8.34 ± 0.62		7.82 ± 0.28	
$He^+/H^+ \times 10^2$	7.43 ± 0.54		7.74 ± 0.30	
ICF(He)	1.18		1.25	
He/H $\times 10^2$	8.80 ± 0.64		9.68 ± 0.38	

Table 6. Summary of knot properties.

Property	Knot A	Knot B	Knot C
Ly α emitter	\times	\times	\checkmark
WR population	5200 ± 1500	900 ± 400	300 ± 400
N_{WR}/N_{WR+O}	~ 0.020	~ 0.014	~ 0.012
SF age (Myr)	4.9 ± 0.4	4.3 ± 0.5	7.4 ± 0.3
Current SFR ($M_{\odot} \text{ yr}^{-1}$)	0.26	0.86	0.09
$12+\log(O/H)$	8.09 ± 0.20	8.25 ± 0.15	7.80 ± 0.13
$\log(N/O)$	-1.41 ± 0.08	-1.28 ± 0.06	-1.12 ± 0.05

6 WR STARS AND N-ENRICHMENT

As discussed previously, a connection is thought to exist between galaxies with high N/O ratios and the presence of WR stars (e.g. Brinchmann, Kunth & Durret 2008, and references therein). Two examples are NGC 5253 (López-Sánchez et al. 2007, and references therein) and Mrk 996 (James et al. 2009), where spatially resolved studies showed regions of enhanced N/O that correlate with a strong WR population. However, the relationship may not be clear-cut. Cases also exist where galaxies display N-overabundance over areas too large for WR stars to pollute, suggesting that other mechanisms may be responsible (Pérez-Montero et al. 2011; James et al. 2013).

The presence of WR features within the spectra of Haro 11 was reported by Bergvall & Östlin (2002). However, to date, no attempt has been made to map or quantify the size of this population. The FLAMES-IFU spectra also show a broad WR stellar feature around 4690 Å, attributable to a mixture of late-type WN (WNL) stars, as seen in Fig. 10. A map of the WR feature is shown in Fig. 11 (made by integrating the flux across the feature), where the WR emission is seen to extend throughout Knots A and B, with only a minimal detection in Knot C.

When searching for WR features one must consider the spatial width of the extraction aperture, which can sometimes be too large and thereby dilute weak WR features with continuum flux (Kehrig et al. 2008; López-Sánchez & Esteban 2008; James et al. 2010; Pérez-Montero et al. 2011). We therefore also examined the spectra summed over each individual knot (Fig. 2), which are shown in Fig. 10. In order to determine the number of WR stars from the strength of the 4640–4690 Å feature for the summed spectra over Knots A, B and C, we followed the procedure described in James et al. (2013). This makes use of a Large Magellanic Cloud WR (WN5–6) spectral template from Crowther & Hadfield (2006) to fit the observed WR broad feature using Monte Carlo to estimate the errors.

It is thus estimated that 900 ± 400 , 1500 ± 300 and 300 ± 400 WN stars are present in Knots A, B and C, respectively. A total

population of 5200 ± 1500 WN stars is estimated by applying the same procedure for the integrated spectrum of the entire galaxy. The difference between this and the total number of WR stars from the regional spectra suggests that there may be WR stars located outside knots of star formation, similar to the situation in the nearby BCG NGC 5253 (e.g. Monreal-Ibero et al. 2010, and references therein).

Due to the short WR phase of a star’s evolution, another way to assess if they are present is to estimate the current age of the ionizing stellar population. This can be achieved by assessing the EW of $H\beta$ at a given metallicity. A map of EW($H\beta$) is shown in Fig. 12. Two regions of increased EW are present, located at Knots A and B. Knot C, on the other hand, shows a distinct decrease in EW. Following the method outlined in James et al. (2010), we can use this map, in conjunction with the metallicity map described in Section 5.1, to estimate the age of the most recent star-forming episodes throughout Haro 11, by comparing the regional observed average EW($H\beta$) values with those predicted by the spectral synthesis code STARBURST99 (Leitherer et al. 1999). We utilize the same model parameters described in James et al. (2010) and obtain average stellar ages of 4.9 ± 0.4 , 4.3 ± 0.5 and 7.4 ± 0.3 Myr for Knots A, B and C, respectively. These ages are in relatively good agreement

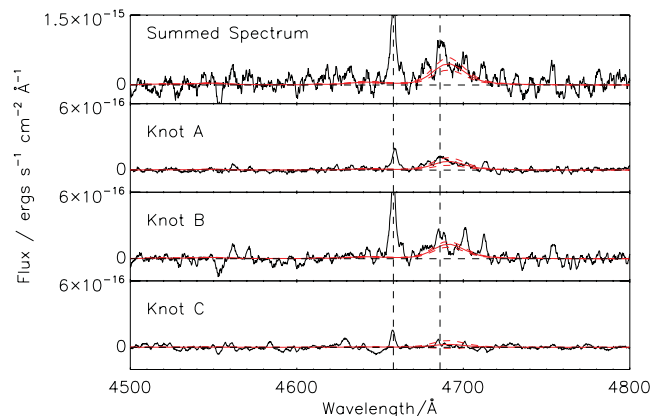


Figure 10. Sections of continuum-subtracted FLAMES IFU spectra, showing the blue ‘WR bump’ region within summed spectra over the entire galaxy and separate aperture regions 1, 2 and 3 (see Fig. 2). We detect WR emission features in the spectra summed over the entire galaxy and also each of the individual aperture region spectra. Overlaid are the estimates of 5200 ± 1500 , 900 ± 400 , 1500 ± 300 and 300 ± 400 WN stars, for the entire galaxy and Knots A, B and C, respectively, using the templates of Crowther & Hadfield (2006). The vertical dashed lines indicate the location of [Fe III] 4658 Å and a weak, narrow, He II emission line at 4686 Å. The dashed horizontal lines in the plots show the zero flux levels.

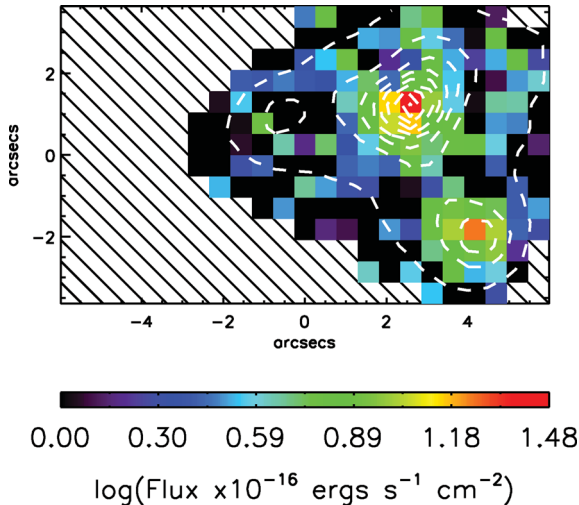


Figure 11. Emission map of the blue WR feature, showing the distribution of WR stars throughout Haro 11. Overlaid dashed contours represent the $H\alpha$ integrated flux. North is up and east is to the left.

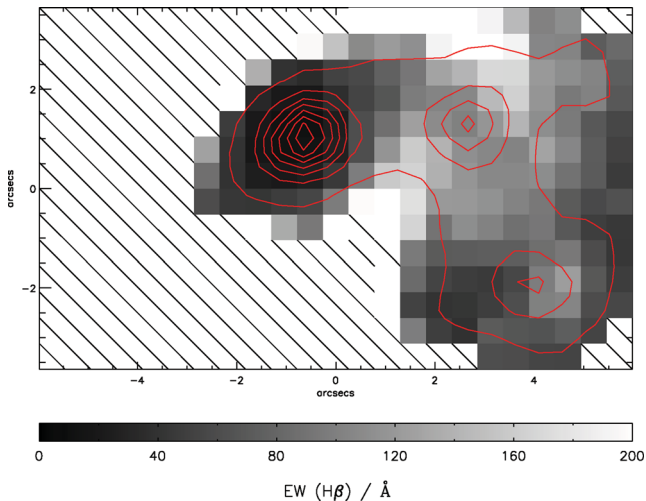


Figure 12. Map of the EW of $H\beta$ across Haro 11. Overlaid red lines are contours of $H\beta$ -region continuum. North is up and east is to the left.

with Adamo et al. (2010) who derive ages of 3.9 and 9.5 Myr for Knots B and C, respectively, from modelled spectral energy distributions of the star clusters. According to Leitherer et al. (1999), typically an instantaneous starburst shows WR features at ages of ~ 3 – 6 Myr for metallicities of $Z = 0.004$ – 0.008 , similar to those seen in Haro 11. Thus, the stellar population ages of Knots A and B are consistent with hosting WR stars, whilst Knot C appears too old to do so.

Due to their high mass, the number ratio of WR stars to O stars within a galaxy can be used to provide constraints on the high-mass end of the initial mass function (IMF). Following the methodology outlined in James et al. (2009), an estimation of the number of O-type stars within each knot was made using $L(H\beta)$, N_{WR} and the number of O7V equivalent stars (e.g. Kunth & Sargent 1981; Osterbrock & Cohen 1982), after applying the appropriate correction factor for the proportion of other O-star subtypes, $\eta_0(t)$, for the metallicity of each knot. The emission rates of ionizing photons, Q_0^{obs} , are 1.01, 3.20 and 0.34×10^{53} photons s^{-1} for Knots A, B and C, respectively, yielding average O-star popula-

tions of size $\sim 45\,900$, $\sim 101\,700$ and $\sim 25\,800$. As a result, we find N_{WR}/N_{WR+O} ratios of 0.020, 0.014 and 0.012 for Knots A–C. These results are in agreement with the predictions of Schaerer & Vacca (1998) for Knots A and C, but for an IMF with $\alpha = 3.0$ (see López-Sánchez & Esteban 2010a, their fig. 13), i.e. slightly steeper than the Salpeter-like IMF with $\alpha = 2.35$. However, the ratio for Knot B calls for an even steeper IMF. One must bear in mind that here we are assuming $N_{WR} = N_{WNL}$ and, as López-Sánchez & Esteban (2010a) point out, the inclusion of WCE stars may increase the N_{WR}/N_{WR+O} ratio sufficiently to reconcile our results with the standard Salpeter IMF.

By comparing the map of N/O (Fig. 9) and WR emission (Fig. 11) we are thus faced with two intriguing situations. First, for Knot C, we have a large area of gas with a relatively high N/O ratio and a small WR population, and secondly, for Knots A and B, we have the reverse situation; regions with relatively low N/O ratios but large WR populations. In the following, we will discuss scenarios that may explain these circumstances (for guidance, we summarize the main properties of each knot in Table 6).

Knot C: the negligible amount of WR emission within this region combined with the large projected area of high N/O suggests that N-rich winds may not be the cause of the observed $\Delta \log(N/O) \sim +0.5$ dex excess. Whilst this enrichment may be related to the stellar wind ejecta coming from WR stars in neighbouring Knot B, the ~ 1 kpc separation distance between Knot B’s peak in WR emission and the Knot C region of enhanced N/O suggests that this is unlikely. Instead, the excess may be due to other global processes occurring in Haro 11. For example, the galaxy’s unrelaxed dynamics suggests that it is a merger of two bodies. Indeed, the differing age, N_e , T_e and metallicity of Knot C compared to the rest of Haro 11 (see Table 6) suggest that it has undergone a separate evolutionary path.

The decreased oxygen abundance in Knot C indicates that accretion of metal-poor gas might be implicated; some studies suggest that interacting galaxies fall ~ 0.2 dex below the mass–metallicity relation of normal galaxies due to tidally induced large-scale metal-poor gas inflow to the galaxies’ central regions (e.g. Kewley, Geller & Barton 2006; Michel-Dansac et al. 2008; Peeples, Pogge & Stanek 2009). However, the stellar mass of Knot C ($1.36 \times 10^7 M_\odot$; Adamo et al. 2010) and its map-derived average metallicity ($12 + \log(O/H) = 7.8 \pm 0.13$) actually place it in direct agreement with the M – Z relationship at low masses (see Zahid et al. 2012, their fig. 6), i.e. alongside low-mass dwarf irregulars from Lee et al. (2006) and other blue compact dwarf (BCD) galaxies from Zhao, Gao & Gu (2010).

Conversely, there may have been an outflow of oxygen-enriched gas due to SNe (see e.g. van Zee & Haynes 2006), rather than an inflow of metal-poor gas. The effective yield of oxygen and nitrogen may not be in sync since the former is formed in high-mass stars, and the latter in intermediate-mass stars, and it is the more recently enriched gas that is ejected via SN winds (e.g. the case of NGC 1569; Martin, Kobulnicky & Heckman 2002). Indeed, being 2–3 Myr older than the rest of the galaxy, Knot C may have experienced more SN explosions than the younger knots, A and B. This scenario might be more plausible with the aforementioned top-heavy IMF that is required to explain the number ratio of WR/O stars.

Alternatively, the age of Knot C (7.4 Myr) implies that its WR phase has recently been completed, whereas in Knots A and B (both with ages of ~ 4 – 5 Myr) the WR phase is still ongoing. This suggests that Knot C has had sufficient time to maximize the injection of N into the local ISM during its WR phase, which may still be relatively undiluted by subsequent mass-loss of lower mass stars. This case

is supported by Knot C having a lower current SFR [$\sim 0.09 M_{\odot} \text{ yr}^{-1}$, as derived from the $H\alpha$ flux listed in Table 5 and the Kennicutt (1998) relationship], in comparison to Knot B ($0.86 M_{\odot} \text{ yr}^{-1}$) and Knot A ($0.26 M_{\odot} \text{ yr}^{-1}$). The situation witnessed here, where the mixed ejecta have cooled but the WR phase has finished, confirms that the relationship between N-enrichment and the existence of WR features is far from being one-to-one. In fact, Haro 11 is highly analogous to the nearby ‘high-N/O’ BCD NGC 5253, where N-enrichment is not always directly associated with the presence of WR stars (Monreal-Ibero et al. 2010; Westmoquette et al. 2012). As more spatially resolved analyses come to light on ‘high-N/O objects’, it is becoming apparent that the simultaneous detection of both WR features and enhanced N/O is most probably a function of starburst age and the properties of the surrounding medium. As proposed by Westmoquette et al. (2012), in the two known cases where an increase in N/O is coupled with a WR population, i.e. ‘Knot 1’ in NGC 5253 (Monreal-Ibero et al. 2012, and references therein) and the central region of Mrk 996 (James et al. 2009), we are only able to observe the enriched gas because the high density and pressure of the ISM surrounding these areas may have acted to impede the WR winds, allowing their metal-enriched ejecta to mix with the cooler phases and subsequently become detectable in the warm ($\sim 10^4$ K) gas.

Knots A+B: the existence of a strong WR population within these knots, but at normal levels of N/O, suggest that we are observing the galaxy at an interesting point in its evolutionary path. This situation has also been observed in NGC 5253 (see results for ‘Knot # 2’ of Monreal-Ibero et al. 2012), where WR features were seen in a region of clusters $\sim 1\text{--}5$ Myr in age, with normal N/O levels for its metallicity. Here the authors suggest that we are observing a region whose stars are in the process of expelling their processed nitrogen (which begins $\lesssim 5$ Myr) and have not had enough time for this material to cool down and mix with the ISM. Under the assumptions of instantaneous mixing and that the velocity of this gas traces the velocity for which the contamination of extra nitrogen propagates through the ISM, they estimated that the cooling down and mixing of expelled material can last between ~ 2 and 8 Myr over an area 40–50 pc in diameter. For comparison, the areas of Knots A and B are ~ 0.4 and ~ 1 kpc², respectively. If this injection of extra nitrogen takes place as early as ~ 2.5 Myr (according to the models of Mollá & Terlevich 2012), the N-enriched material has had only ~ 2 Myr to be expelled, mixed and diluted in the ISM across these regions.

In addition to the timing of these observations, we should also consider that our limited spatial resolution may be a factor. Even for nearby 30 Doradus that contains Of- and WR-type stars, nitrogen self-enrichment in that nebula has not been detected with any certainty (Rosa & Mathis 1987), and the H_{II} region overall shows a normal N/O ratio for its $0.5 Z_{\odot}$ metallicity (Tsamis et al. 2003; Tsamis & Péquignot 2005).

7 SUMMARY AND CONCLUSIONS

We have analysed FLAMES-IFU integral field spectroscopy of Haro 11, a BCG well known for its high star-formation efficiencies and Ly α emission, making it analogous to the high-redshift LBGs. We have studied its morphology by creating monochromatic emission line maps. The galaxy is seen to consist of three star-forming knots (named A, B and C), arranged in the shape of a heart with Knot B, the region of strongest $H\alpha$ surface brightness in the centre, and Knots A and C to the east and south-east, respectively. Haro 11

exhibits complex emission line profiles, with most lines consisting of a narrow, central component, an underlying broad component and a third narrow component. In agreement with previous studies of $H\alpha$ kinematics, this system is not dynamically relaxed and is possibly an ongoing merger. In particular, the contrasting kinematics of the broad and narrow emission line components suggest the presence of a counter-rotating disc within the central region of the galaxy.

For the first time we present 200 pc resolution maps of T_e , N_e , and the abundance ratios of O/H, N/H, Ne/H and S/H across Haro 11. The abundance maps were derived using the direct method of estimating electron temperature from the $[O III] \lambda 4363/\lambda 4959$ line ratio.

Variations in oxygen abundance are seen across Haro 11 in the narrow emission component, with a peak in abundance of $12 + \log(O/H) = 8.25 \pm 0.15$ in Knot B, decreasing to 8.09 ± 0.23 and 7.80 ± 0.13 in Knots A and C, respectively. We measured a difference of ~ 2000 K between the temperature of the broad and narrow line emission regions in Knot B, but the spectral resolution of our data is not sufficiently high to allow the decomposition of $[O III]$ in the broad regions. Thus, the total oxygen abundance differential between the two gas phases remains unknown.

The low O/H abundance ratio in Knot C tallies with the increased T_e in that region. We detect a high N/O ratio (previously reported for the whole galaxy; Izotov & Thuan 1999) only in Knot C, with $\Delta \log(N/O) \sim +0.5$ dex, spatially coincident with the decrease in oxygen abundance. This knot also shows a distinctly lower N_e in comparison to the rest of the galaxy. This may relate to the previously reported Ly α emission observed solely from this region.

We assess the reliability of abundances derived from galaxy integrated spectra by comparing those derived from integrated spectra with spatial averages. Whilst abundances relative to oxygen are consistent within the uncertainties, abundances relative to hydrogen are not. These results illustrate the superior information content of abundances from spatially resolved spectra.

Using the 4686 Å WR signature, we detect evidence of a large WR population in Knots A and B. No evidence for WR stars was found in Knot C, although we do measure an enhanced N/O and a decreased O/H ratio. This leads us to believe that the abundance anomaly in this region may be due to a recently completed WR phase where N remains undiluted by subsequent mass-loss of lower mass stars. The strong WR emission in Knots A+B combined with ‘normal’ N/O levels and a young stellar population (< 5 Myr) suggest that we are observing these knots at an epoch where ejected N-rich material is yet to mix with the warm ionized gas. Alternatively, even the spatial resolution of these data (0.52 arcsec spaxel⁻¹), corresponding to ~ 210 pc at the distance of Haro 11), may be preventing us from detecting small-scale N-enhancements that have already formed.

To conclude, the IFS data presented in this study show the complexity of Haro 11 as a system; not only is it complicated kinematically but also chemically. In order to better understand the evolution of this system, the inhomogeneous conditions and metallicity of its ISM exposed by our chemodynamical study need to be combined with its star-formation history in models. Observations at even higher resolution are required to constrain the mixing time-scales of the ejecta from its large WR population. Successful modelling of an LBG analogue such as this could have a significant impact on our understanding of the chemical homogeneity, ISM mixing, and effect of feedback on galaxy evolution in both the local and high- z universe.

ACKNOWLEDGEMENTS

We would like to thank the FLAMES staff at Paranal and Garching for scheduling and taking these service mode observations [programme 083.B-0336A; PI: B. L. James]. We thank the referee for a careful reading of the manuscript and a constructive report. We appreciate discussions with Ana Monreal-Ibero regarding theories of N-enrichment from WR stars. YGT acknowledges support from a Marie Curie Intra-European Fellowship within the 7th European Community Framework Programme (grant agreement PIEF-GA-2009-236486). BLJ acknowledges support from an STScI-DDRF travel grant used to visit collaborators of this study. This research made use of the NASA ADS and NED data bases.

REFERENCES

- Adamo A., Östlin G., Zackrisson E., Hayes M., Cumming R. J., Micheva G., 2010, *MNRAS*, 407, 870
- Amorín R., Vílchez J. M., Hägele G. F., Firpo V., Pérez-Montero E., Papaderos P., 2012, *ApJ*, 754, L22
- Benjamin R. A., Skillman E. D., Smits D. P., 1999, *ApJ*, 514, 307
- Bergvall N., Östlin G., 2002, *A&A*, 390, 891
- Bergvall N., Masegosa J., Östlin G., Cernicharo J., 2000, *A&A*, 359, 41
- Blecha A., Simond G., 2004, *GIRRAFE BLDR Software Reference Manual*, available at: <http://girbldrs.sourceforge.net>
- Brinchmann J., Kunth D., Durret F., 2008, *A&A*, 485, 657
- Cormier D. et al., 2012, *A&A*, 548, A20
- Crowther P. A., Hadfield L. J., 2006, *A&A*, 449, 711
- DeBernardis F., Melchiorri A., Verde L., Jimenez R., 2008, *J. Cosmol. Astropart. Phys.*, 3, 20
- Esteban C., Vílchez J. M., 1992, *ApJ*, 390, 536
- Grimes J. P. et al., 2007, *ApJ*, 668, 891
- Guseva N. G., Izotov Y. I., Fricke K. J., Henkel C., 2012, *A&A*, 541, A115
- Hägele G. F., Firpo V., Bosch G., Díaz Á. I., Morrell N., 2012, *MNRAS*, 422, 3475
- Hayes M., Östlin G., Atek H., Kunth D., Mas-Hesse J. M., Leitherer C., Jiménez-Bailón E., Adamo A., 2007, *MNRAS*, 382, 1465
- Hayes M. et al., 2010, *Nat*, 464, 562
- Howarth I. D., 1983, *MNRAS*, 203, 301
- Izotov Y. I., Thuan T. X., 1999, *ApJ*, 511, 639
- Izotov Y. I., Stasińska G., Meynet G., Guseva N. G., Thuan T. X., 2006, *A&A*, 448, 955
- James B. L., Tsamis Y. G., Barlow M. J., Westmoquette M. S., Walsh J. R., Cuisinier F., Exter K. M., 2009, *MNRAS*, 398, 2
- James B. L., Tsamis Y. G., Barlow M. J., 2010, *MNRAS*, 401, 759
- James B. L., Tsamis Y. G., Barlow M. J., Walsh J. R., Westmoquette M. S., 2013, *MNRAS*, 428, 86
- Kehrig C., Vílchez J. M., Sánchez S. F., Telles E., Pérez-Montero E., Martín-Gordón D., 2008, *A&A*, 477, 813
- Kennicutt R. C., Jr, 1998, *ARA&A*, 36, 189
- Kewley L. J., Geller M. J., Barton E. J., 2006, *AJ*, 131, 2004
- Kingsburgh R. L., Barlow M. J., 1994, *MNRAS*, 271, 257
- Kobulnicky H. A., Kennicutt R. C., Jr, Pizagno J. L., 1999, *ApJ*, 514, 544
- Kunth D., Sargent W. L. W., 1981, *A&A*, 101, L5
- Kunth D., Mas-Hesse J. M., Terlevich E., Terlevich R., Lequeux J., Fall S. M., 1998, *A&A*, 334, 11
- Kunth D., Leitherer C., Mas-Hesse J. M., Östlin G., Petrosian A., 2003, *ApJ*, 597, 263
- Lee H., Skillman E. D., Cannon J. M., Jackson D. C., Gehrz R. D., Polomski E. F., Woodward C. E., 2006, *ApJ*, 647, 970
- Leitet E., Bergvall N., Piskunov N., Andersson B.-G., 2011, *A&A*, 532, A107
- Leitherer C. et al., 1999, *ApJS*, 123, 3
- Lennon D. J., Burke V. M., 1994, *A&AS*, 103, 273
- López-Sánchez Á. R., Esteban C., 2008, *A&A*, 491, 131
- López-Sánchez Á. R., Esteban C., 2010a, *A&A*, 516, A104
- López-Sánchez Á. R., Esteban C., 2010b, *A&A*, 517, A85
- López-Sánchez Á. R., Esteban C., García-Rojas J., Peimbert M., Rodríguez M., 2007, *ApJ*, 656, 168
- Martin C. L., Kobulnicky H. A., Heckman T. M., 2002, *ApJ*, 574, 663
- Mas-Hesse J. M., Kunth D., Tenorio-Tagle G., Leitherer C., Terlevich R. J., Terlevich E., 2003, *ApJ*, 598, 858
- McLaughlin B. M., Bell K. L., 1993, *ApJ*, 408, 753
- Michel-Dansac L., Lambas D. G., Alonso M. S., Tissera P., 2008, *MNRAS*, 386, L82
- Mollá M., Terlevich R., 2012, *MNRAS*, 425, 1696
- Monreal-Ibero A., Vílchez J. M., Walsh J. R., Muñoz-Tuñón C., 2010, *A&A*, 517, A27
- Monreal-Ibero A., Walsh J. R., Vílchez J. M., 2012, *A&A*, 544, A60
- Neufeld D. A., 1991, *ApJ*, 370, L85
- Osterbrock D. E., Cohen R. D., 1982, *ApJ*, 261, 64
- Osterbrock D. E., Ferland G. J., 2006, *Astrophysics of Gaseous Nebulae and Active Galactic Nuclei*. University Science Books, Mill Valley, CA
- Östlin G., Amram P., Masegosa J., Bergvall N., Boulesteix J., 1999, *A&AS*, 137, 419
- Östlin G., Amram P., Bergvall N., Masegosa J., Boulesteix J., Márquez I., 2001, *A&A*, 374, 800
- Pasquini L. et al., 2002, *The Messenger*, 110, 1
- Peebles M. S., Pogge R. W., Stanek K. Z., 2009, *ApJ*, 695, 259
- Peimbert M., Costero R., 1969, *Bol. Obs. Tonantzintla Tacubaya*, 5, 3
- Peimbert M., Torres-Peimbert S., Ruiz M. T., 1992, *Rev. Mex. Astron. Astrofis.*, 24, 155
- Pérez-Montero E. et al., 2011, *A&A*, 532, A141
- Pilyugin L. S., Vílchez J. M., Mattsson L., Thuan T. X., 2012, *MNRAS*, 421, 1624
- Pustilnik S., Kniazev A., Pramskij A., Izotov Y., Foltz C., Brosch N., Martin J.-M., Ugryumov A., 2004, *A&A*, 419, 469
- Rosa M., Mathis J. S., 1987, *ApJ*, 317, 163
- Rubin R. H., 1989, *ApJS*, 69, 897
- Schaerer D., Vacca W. D., 1998, *ApJ*, 497, 618
- Schlegel D. J., Finkbeiner D. P., Davis M., 1998, *ApJ*, 500, 525
- Smits D. P., 1996, *MNRAS*, 278, 683
- Storey P. J., Hummer D. G., 1995, *MNRAS*, 272, 41
- Tsamis Y. G., Péquignot D., 2005, *MNRAS*, 364, 687
- Tsamis Y. G., Barlow M. J., Liu X.-W., Danziger I. J., Storey P. J., 2003, *MNRAS*, 338, 687
- Tsamis Y. G., Walsh J. R., Péquignot D., Barlow M. J., Danziger I. J., Liu X.-W., 2008, *MNRAS*, 386, 22
- Vader J. P., Frogel J. A., Terndrup D. M., Heisler C. A., 1993, *AJ*, 106, 1743
- van Zee L., Haynes M. P., 2006, *ApJ*, 636, 214
- Viegas S. M., Clegg R. E. S., 1994, *MNRAS*, 271, 993
- Walsh J. R., Roy J.-R., 1989, *MNRAS*, 239, 297
- Walsh J. R., Roy J. R., in Baade D., Grosbol P. J., eds, *ESO Conf. Proc. Vol. 34, 2nd ESO/ST-ECF Data Analysis Workshop*. p. 95, available at: <http://adsabs.harvard.edu/abs/1990ESOC...34...95W>
- Westmoquette M. S., Smith L. J., Gallagher J. S., III, 2011, *MNRAS*, 414, 3719
- Westmoquette M. S., James B. L., Monreal-Ibero A., Walsh J. R., 2012, *A&A*, (arXiv:1212.2385)
- Wiese W. L., Fuhr J. R., Deters T. M., 1996, in Wiese W. L., Fuhr J. R., Deters T. M., eds, *Atomic Transition Probabilities of Carbon, Nitrogen, and Oxygen : A Critical Data Compilation*. AIP, New York
- Zahid H. J., Bresolin F., Kewley L. J., Coil A. L., Davé R., 2012, *ApJ*, 750, 120
- Zhao Y., Gao Y., Gu Q., 2010, *ApJ*, 710, 663

APPENDIX A: REGIONAL OBSERVED FLUXES AND LINE INTENSITIES

Tables A1–A3 list the observed fluxes and de-reddened line intensities derived from summed spectra over the regions defined in Fig. 2. Fluxes are given for each separate velocity component (C1–C3), along with its de-reddened line intensity and FWHM.

Table A1. Haro 11 regional fluxes and de-reddened line intensities (both relative to $H\beta = 100$) and FWHMs (in km s^{-1}) for summed spectra over Knot A (as defined in Fig. 2). Line fluxes were extinction-corrected using the $c(H\beta)$ values shown at the bottom of the table, calculated from the relative $H\alpha$, $H\beta$ and $H\gamma$ fluxes.

Knot A	C1			C2		
	$F(\lambda)$	$I(\lambda)$	FWHM	$F(\lambda)$	$I(\lambda)$	FWHM
[O II] $\lambda 3727$	299.97 ± 11.85	315.67 ± 13.40	176.47 ± 0.83			
[O II] $\lambda 3729$	296.16 ± 11.73	311.66 ± 13.26	176.36 ± 0.83			
[Ne III] $\lambda 3868$	111.34 ± 5.18	116.58 ± 5.70	158.20 ± 4.17			
H8+He I $\lambda 3889$	64.33 ± 4.24	67.32 ± 4.55	168.31 ± 8.94			
He I $\lambda 4026$	3.00 ± 0.28	3.12 ± 0.29	126.20 ± 10.69			
[S II] $\lambda 4068$	2.39 ± 0.28	2.48 ± 0.29	124.34 ± 14.69			
H δ	43.23 ± 2.65	44.82 ± 2.83	120.78 ± 2.68	19.37 ± 1.63	19.58 ± 1.69	247.11 ± 8.02
H γ	47.49 ± 4.10	48.70 ± 4.26	80.30 ± 4.40	45.58 ± 1.84	45.91 ± 2.05	251.43 ± 6.14
[O III] $\lambda 4363$	6.15 ± 1.63	6.30 ± 1.68	121.07 ± 18.29	2.28 ± 1.49	2.27 ± 1.48	318.69 ± 128.11
He I $\lambda 4471$	6.23 ± 1.39	6.35 ± 1.42	117.51 ± 11.21	2.34 ± 0.99	2.35 ± 1.00	245.70 ± 54.33
[Fe III] $\lambda 4657$	3.50 ± 0.46	3.54 ± 0.47	213.39 ± 26.67			
H β	100.00 ± 5.53	100.00 ± 5.60	80.28 ± 2.20	100.00 ± 2.21	100.00 ± 2.78	253.78 ± 2.57
[O III] $\lambda 4959$	143.94 ± 7.60	143.25 ± 7.66	72.61 ± 1.81	127.54 ± 3.36	125.70 ± 3.01	255.08 ± 2.23
[O I] $\lambda 6364$	2.15 ± 0.13	2.03 ± 0.12	164.21 ± 7.27			
[N II] $\lambda 6548$	6.70 ± 0.37	6.29 ± 0.35	62.58 ± 2.20	10.51 ± 0.24	10.32 ± 0.27	276.55 ± 5.03
H α	317.46 ± 13.38	298.32 ± 12.82	81.42 ± 0.77	288.62 ± 4.64	283.56 ± 5.62	263.30 ± 0.53
[N II] $\lambda 6584$	24.97 ± 1.06	23.41 ± 1.01	74.61 ± 1.09	28.68 ± 0.52	28.146 ± 0.60	259.11 ± 2.11
He I $\lambda 6678$	2.85 ± 0.31	2.66 ± 0.29	67.35 ± 4.69	3.00 ± 0.27	2.95 ± 0.27	259.27 ± 19.96
[S II] $\lambda 6716$	10.84 ± 0.61	10.13 ± 0.59	72.78 ± 2.19	15.37 ± 0.35	15.08 ± 0.38	239.06 ± 2.35
$c(H\beta)$		0.09 ± 0.01			0.02 ± 0.01	
$F(H\beta) \times 10^{14} \text{ erg s}^{-1} \text{ cm}^{-2}$		1.99 ± 0.08			2.73 ± 0.04	

	$F(\lambda)$	C3 $I(\lambda)$	FWHM
[O II] $\lambda 3727$			
[O II] $\lambda 3729$			
[Ne III] $\lambda 3868$			
H8+He I $\lambda 3889$			
He I $\lambda 4026$			
[S II] $\lambda 4068$			
H δ			
H γ	43.92 ± 8.93	44.61 ± 9.97	58.48 ± 5.17
[O III] $\lambda 4363$			
He I $\lambda 4471$			
[Fe III] $\lambda 4657$			
H β	100.00 ± 12.14	100.00 ± 14.54	57.76 ± 2.51
[O III] $\lambda 4959$	171.58 ± 18.76	165.52 ± 20.61	59.28 ± 2.15
[O I] $\lambda 6364$			
[N II] $\lambda 6548$	5.57 ± 0.71	5.35 ± 0.75	49.33 ± 3.28
H α	288.47 ± 27.36	276.75 ± 30.48	62.37 ± 1.11
[N II] $\lambda 6584$	12.48 ± 1.30	11.96 ± 1.41	42.66 ± 1.71
He I $\lambda 6678$	3.78 ± 0.76	3.62 ± 0.75	58.65 ± 5.99
[S II] $\lambda 6716$	13.14 ± 1.49	13.14 ± 1.84	52.72 ± 2.07
$c(H\beta)$		0.06 ± 0.04	
$F(H\beta) \times 10^{14} \text{ erg s}^{-1} \text{ cm}^{-2}$		0.86 ± 0.07	

Table A2. Same as for Table A1, for summed spectra over Knot B (as defined in Fig. 2).

Knot B	C1			C2		
	$F(\lambda)$	$I(\lambda)$	FWHM	$F(\lambda)$	$I(\lambda)$	FWHM
[O II] λ 3727	344.56 \pm 8.92	469.13 \pm 44.25	256.33 \pm 17.33			
[O II] λ 3729	355.21 \pm 9.19	483.63 \pm 45.61	256.11 \pm 17.32			
[Ne III] λ 3868	87.79 \pm 2.96	115.98 \pm 11.03	212.82 \pm 4.82			
H8+He I λ 3889	59.32 \pm 2.76	78.09 \pm 7.82	209.83 \pm 8.22			
He I λ 4026	4.01 \pm 0.20	5.09 \pm 0.51	172.42 \pm 7.98			
[S II] λ 4068	4.58 \pm 0.24	5.75 \pm 0.58	188.22 \pm 8.86			
H δ	24.43 \pm 1.31	30.42 \pm 3.07	121.96 \pm 2.80	24.06 \pm 0.60	24.76 \pm 1.72	296.04 \pm 4.70
Fe II λ 4286	1.69 \pm 0.32	2.00 \pm 0.41	213.13 \pm 42.98			
H γ	39.50 \pm 2.51	46.04 \pm 4.75	121.30 \pm 3.00	46.56 \pm 1.23	47.50 \pm 3.19	298.60 \pm 4.44
[O III] λ 4363	3.60 \pm 0.66	4.17 \pm 0.83	132.66 \pm 17.21	2.69 \pm 0.57	2.68 \pm 0.57	412.75 \pm 110.16
He I λ 4471	4.78 \pm 0.46	5.37 \pm 0.67	122.62 \pm 6.51	3.51 \pm 0.22	3.56 \pm 0.31	384.48 \pm 28.20
[Fe III] λ 4657	4.47 \pm 0.28	4.75 \pm 0.46	204.16 \pm 11.96			
H β	100.00 \pm 3.57	100.00 \pm 8.06	118.66 \pm 1.63	100.00 \pm 1.63	100.00 \pm 5.71	290.99 \pm 2.21
[O III] λ 4959	118.11 \pm 3.62	114.74 \pm 8.82	104.61 \pm 1.16	116.51 \pm 6.43	111.89 \pm 4.68	276.68 \pm 1.47
[O I] λ 6364	2.06 \pm 0.20	1.47 \pm 0.16	119.18 \pm 5.77	1.99 \pm 0.10	1.91 \pm 0.12	325.55 \pm 16.60
[N II] λ 6548	13.61 \pm 0.61	9.28 \pm 0.62	89.60 \pm 1.55	14.41 \pm 0.28	13.71 \pm 0.58	200.66 \pm 2.06
H α	417.83 \pm 10.80	286.85 \pm 16.06	125.02 \pm 0.41	306.78 \pm 3.67	292.02 \pm 11.54	294.78 \pm 0.41
[N II] λ 6584	56.97 \pm 1.59	38.59 \pm 2.17	100.03 \pm 0.70	55.54 \pm 0.69	52.77 \pm 2.06	264.94 \pm 1.21
He I λ 6678	2.80 \pm 0.22	1.87 \pm 0.17	91.73 \pm 3.41	3.92 \pm 0.10	3.72 \pm 0.16	242.46 \pm 6.23
[S II] λ 6716	15.05 \pm 0.50	9.96 \pm 0.58	97.79 \pm 1.26	25.50 \pm 0.33	24.16 \pm 0.93	253.33 \pm 1.00
$c(\text{H}\beta)$		0.52 \pm 0.03			0.07 \pm 0.02	
$F(\text{H}\beta) \times 10^{14} \text{ erg s}^{-1} \text{ cm}^{-2}$		5.83 \pm 0.15			11.88 \pm 0.14	

Table A3. Same as for Table A1, for summed spectra over Knot C (as defined in Fig. 2).

Knot C	C1			C2		
	$F(\lambda)$	$I(\lambda)$	FWHM	$F(\lambda)$	$I(\lambda)$	FWHM
[O II] λ 3727	208.00 \pm 9.85	245.20 \pm 28.29	125.59 \pm 0.72			
[O II] λ 3729	263.87 \pm 12.46	311.07 \pm 35.88	125.47 \pm 0.72			
[Ne III] λ 3868	53.77 \pm 4.66	62.38 \pm 8.40	125.33 \pm 10.34			
H8+He I λ 3889	19.62 \pm 4.75	22.71 \pm 5.98	81.12 \pm 21.74			
He I λ 4026	1.20 \pm 0.40	1.36 \pm 0.47	114.56 \pm 40.39			
[S II] λ 4068	6.99 \pm 0.63	7.89 \pm 1.06	135.69 \pm 11.52			
H δ	37.01 \pm 1.84	41.60 \pm 4.61	99.87 \pm 1.73			
Fe II λ 4244	6.65 \pm 1.05	7.32 \pm 1.36	174.51 \pm 26.47			
Fe II λ 4286	8.56 \pm 1.21	9.36 \pm 1.59	188.33 \pm 26.61			
H γ	43.32 \pm 7.81	47.01 \pm 9.57	80.67 \pm 5.68	43.84 \pm 9.31	47.54 \pm 11.10	172.37 \pm 21.11
[O III] λ 4363	6.77 \pm 1.98	7.32 \pm 2.24	185.05 \pm 59.63			
He I λ 4471	3.86 \pm 0.39	4.10 \pm 0.56	82.76 \pm 8.15			
[Fe III] λ 4657	5.37 \pm 0.75	5.55 \pm 0.92	185.77 \pm 26.72			
H β	100.00 \pm 6.58	100.00 \pm 10.65	82.08 \pm 2.13	100.00 \pm 9.40	100.00 \pm 12.74	206.87 \pm 6.83
[O III] λ 4959	109.67 \pm 6.29	107.99 \pm 10.79	81.02 \pm 1.60	101.58 \pm 8.18	100.04 \pm 11.63	213.87 \pm 6.95
[O I] λ 6364	3.08 \pm 0.23	2.58 \pm 0.25	111.20 \pm 6.54			
[N II] λ 6548	11.81 \pm 1.39	9.62 \pm 1.26	67.18 \pm 3.16	17.62 \pm 1.95	14.39 \pm 1.80	147.45 \pm 7.96
H α	355.13 \pm 16.74	290.59 \pm 21.64	97.37 \pm 0.58	357.83 \pm 23.94	293.34 \pm 26.19	286.36 \pm 1.29
[N II] λ 6584	50.24 \pm 2.59	40.82 \pm 3.13	78.31 \pm 1.09	50.36 \pm 3.58	41.00 \pm 3.77	202.66 \pm 4.16
He I λ 6678	4.09 \pm 0.24	3.29 \pm 0.26	88.60 \pm 3.08			
[S II] λ 6716	28.18 \pm 1.60	22.62 \pm 1.79	79.02 \pm 1.38	23.39 \pm 1.94	18.81 \pm 1.89	191.49 \pm 5.89
$c(\text{H}\beta)$		0.28 \pm 0.04			0.28 \pm 0.04	
$F(\text{H}\beta) \times 10^{14} \text{ erg s}^{-1} \text{ cm}^{-2}$		1.07 \pm 0.05			0.81 \pm 0.05	